

# Development of Automated Production Line Processes for Solar Brightfield Modules

**Annual Technical Progress Report  
1 January 2003 – 30 June 2004**

M.J. Nowlan, J.M. Murach, S.F. Sutherland,  
D.C. Miller, S.B. Moore, and S.J. Hogan  
*Spire Corporation  
Bedford, Massachusetts*

**Subcontract Report**  
**NREL/SR-520-36608**  
June 2005

NREL is operated by Midwest Research Institute • Battelle Contract No. DE-AC36-99-GO10337



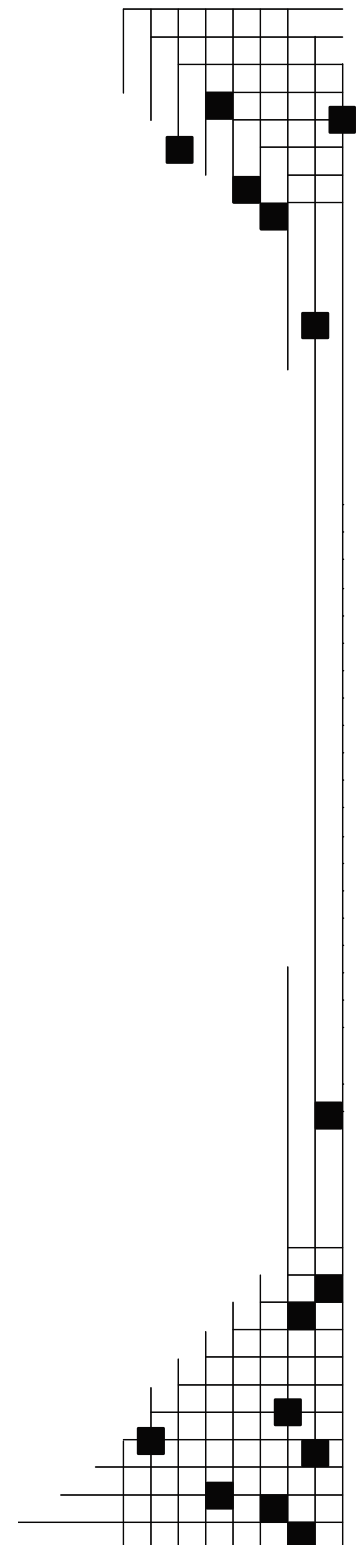
# Development of Automated Production Line Processes for Solar Brightfield Modules

## Annual Technical Progress Report 1 January 2003 – 30 June 2004

M.J. Nowlan, J.M. Murach, S.F. Sutherland,  
D.C. Miller, S.B. Moore, and S.J. Hogan  
*Spire Corporation*  
*Bedford, Massachusetts*

NREL Technical Monitor: K. Brown  
Prepared under Subcontract No. ZDO-3-30628-12

*Subcontract Report*  
NREL/SR-520-36608  
June 2005



**National Renewable Energy Laboratory**  
1617 Cole Boulevard, Golden, Colorado 80401-3393  
303-275-3000 • [www.nrel.gov](http://www.nrel.gov)

Operated for the U.S. Department of Energy  
Office of Energy Efficiency and Renewable Energy  
by Midwest Research Institute • Battelle

Contract No. DE-AC36-99-GO10337

**This publication was reproduced from the best available copy  
Submitted by the subcontractor and received no editorial review at NREL**

### **NOTICE**

This report was prepared as an account of work sponsored by an agency of the United States government. Neither the United States government nor any agency thereof, nor any of their employees, makes any warranty, express or implied, or assumes any legal liability or responsibility for the accuracy, completeness, or usefulness of any information, apparatus, product, or process disclosed, or represents that its use would not infringe privately owned rights. Reference herein to any specific commercial product, process, or service by trade name, trademark, manufacturer, or otherwise does not necessarily constitute or imply its endorsement, recommendation, or favoring by the United States government or any agency thereof. The views and opinions of authors expressed herein do not necessarily state or reflect those of the United States government or any agency thereof.

Available electronically at <http://www.osti.gov/bridge>

Available for a processing fee to U.S. Department of Energy  
and its contractors, in paper, from:

U.S. Department of Energy  
Office of Scientific and Technical Information  
P.O. Box 62  
Oak Ridge, TN 37831-0062  
phone: 865.576.8401  
fax: 865.576.5728  
email: <mailto:reports@adonis.osti.gov>

Available for sale to the public, in paper, from:

U.S. Department of Commerce  
National Technical Information Service  
5285 Port Royal Road  
Springfield, VA 22161  
phone: 800.553.6847  
fax: 703.605.6900  
email: [orders@ntis.fedworld.gov](mailto:orders@ntis.fedworld.gov)  
online ordering: <http://www.ntis.gov/ordering.htm>



# TABLE OF CONTENTS

	<u>Page</u>
1 INTRODUCTION .....	1
1.1 Objective .....	1
1.2 Approach.....	1
2 TECHNICAL DISCUSSION .....	2
2.1 Task 1 – Design Brightfield Module and Production Line .....	2
2.1.1 Brightfield Photovoltaic Module Design .....	2
2.1.2 BOS Electrical Design Analysis .....	7
2.1.3 Production Line Definition .....	8
2.2 Task 2 – Develop Cell String Inspection Process .....	10
2.2.1 Visible Defect Inspections .....	10
2.2.2 Microcrack Inspection.....	13
2.2.3 String Inspection System Integration.....	19
2.3 Task 3 – Develop Advanced Lamination Process.....	21
2.3.1 Faster Curing Encapsulant .....	21
2.3.2 Laminator Cold Trap.....	22
2.3.3 Laminator Heater Thermal Compound .....	24
2.4 Task 4 – Design Module Lay-up System.....	25
2.4.1 Stacking on a Tray .....	25
2.4.2 Winding onto a Tube .....	27
2.4.3 Direct Dispensing onto the Module .....	27
2.5 Task 5 – Design String Busing System.....	29
2.5.1 Bus Ribbon Fabrication .....	29
2.5.2 Bus Ribbon and Diode Installation – SCARA Robot Approach .....	31
2.5.3 Bus Ribbon and Diode Installation – Cartesian Robot Approach.....	32
2.5.4 Automated Soldering Process Development.....	35
3 CONCLUSIONS.....	38

## LIST OF ILLUSTRATIONS

	<u>Page</u>
1 PV sub-arrays at Tucson Electric Power in Springerville, AZ.....	2
2 Diode assembly temperature rise vs. forward current. ....	3
3 Module circuit with laminated diodes and center outputs. ....	4
4 Module circuit with laminated by-pass diodes and end outputs.....	4
5 Isometric views of the Brightfield module design.....	5
6 Bending stress profile under maximum wind and snow load.....	6
7 Steel frame deflection under 113 psf wind and snow load.....	6
8 Module glass and steel deflection under 113 psf wind and snow load.....	7
9 Brightfield module line process flow chart. ....	9
10 Preliminary module production line floor plan for the large area Brightfield module.....	9
11 Automated cell string inspection system with a string of 125 mm cells. ....	10
12 Vision sensor images of a 125 mm polycrystalline silicon cell.....	11
13 Cell front side vision sensor with filter, lamps with reflectors, and backlight .....	11
14 Cell backside vision sensor, LED array, backlight, and mirror.....	12
15 String front side vision inspection tools on a 125 mm polycrystalline Si cell .....	12
16 String back side vision inspection tools with front lighting .....	13
17 String back side vision inspection tools without front lighting.....	13
18 IR images of the back surface of a 125 mm square single-crystal Si solar cell.....	14
19 Cell flexer on test stand. ....	15
20 Prototype cell flexer on test stand with a string of Shell Solar 103 mm cells. ....	16
21 IR images of a 125 mm monocrystalline Si cell with a microcrack .....	17
22 IR images of 103 mm monocrystalline Si cell with a partially soldered interconnect ribbon.....	17
23 Thermal image and software detection of a microcrack in a 125 mm monocrystalline silicon cell....	18
24 Thermal image and soldering inspection results for a 125 mm mono-crystalline silicon cell. ....	18
25 String inspection system integrated with string and module assembly. ....	19
26 Cell string inspection system with a string of 125 mm cells. ....	19
27 Inspection system main window with cell front side camera view selected. ....	20
28 Inspection results window. ....	21
29 Module laminate made with faster-curing EVA.....	22
30 Cold trap and chiller installed on laminator vacuum system.....	23
31 Laminator process chamber pump down with and without a cold trap.....	24
32 Laminator heater test fixture control program GUI.....	25
33 Pick-and-place option for material lay-up in module production.....	26
34 Tedlar sheet (5' x 12') lifted by a vacuum end effector. ....	26
35 End effector with cylinder actuated, cup extended, and bus lead fed through slit. ....	27

36	Prototype sheet unroller.....	27
37	Cover Sheet Applicator for feeding, cutting and dispensing sheet materials.....	28
38	Module conveyor with CSA sheeter configured for EVA dispensing on glass.....	29
39	Mechanical design for the bus ribbon fabrication machine.....	30
40	SCARA robot approach to string busing.....	31
41	Vacuum pick-and-place end effector design for robot arm.....	32
42	Cartesian robot approach to string busing.....	33
43	Bus ribbon tray assembly.....	33
44	Robot end effector with pick-and-place and soldering tools.....	34
45	A robot inserts a bus bar in the bending tool, an air cylinder extends and retracts.....	34
46	Ribbon bender, Spire design.....	35
47	Flux applicator and diode assembly in the module.....	36
48	Preliminary thermode design for string-bus and bus-diode-bus joints.....	36
49	Spire soldering tip assembly.....	37

## LIST OF TABLES

	<u>Page</u>
1 Program tasks. ....	1
2 Nominal specifications for the Brightfield module. ....	3
3 Electrical BOS equipment cost. ....	8
4 Laminate electrical performance at STC. ....	22

# 1 INTRODUCTION

This is Spire Corporation’s Annual Technical Progress Report for Phase 1 of a program entitled “Development of Automated Production Line Processes for Solar Brightfield Modules.” This program is supported by the U. S. Department of Energy under the National Renewable Energy Laboratory’s Photovoltaic Manufacturing R&D (PVMRD) project. Phase 1 efforts extended from January 1, 2003 to June 30, 2004.

## 1.1 Objective

Spire is addressing the PVMRD project goals of improving PV manufacturing processes and products while reducing costs and providing a technology foundation that supports significant manufacturing scale-up. To accomplish this, we are focusing our efforts on the design of a large area utility-scale module and the development of the necessary manufacturing techniques and equipment to manufacture such a module in a high-volume production environment.

## 1.2 Approach

A three-phase program is underway for developing and demonstrating new automated systems for fabricating very large photovoltaic (PV) modules ideal for use in multi-megawatt grid-connected applications. We designed a large area 800 W module and we are developing associated module production equipment that will minimize the total installed system cost for utility-scale PV arrays. Unique features of the module design include a cantilevered glass superstrate to reduce the glass thickness and internally laminated by-pass diodes that simplify internal busing and junction box designs. Other program activities include the development of automation for solar cell string inspections, string busing, materials lay-up, and lamination; enhancements to the lamination process; and performance testing of large area modules. Program tasks are listed in Table 1.

**Table 1 Program tasks.**

Phase	Task
1 – January 03 to June 04	1 Design Brightfield Module and Production Line 2 Develop Cell String Inspection Process 3 Develop Advanced Lamination Process 4 Design Module Lay-up System 5 Design String Busing System
2 - July 04 to June 05	6 Fabricate & Test Module Lay-up System 7 Fabricate & Test String Busing System 8 Design Advanced Lamination Process Tool 9 Design Lamination Automation 10 Design Large Area Solar Simulator
3 - July 05 to June 06	11 Fabricate & Test Advanced Laminator 12 Fabricate & Test Laminator Automation 13 Fabricate & Test Large Area Solar Simulator 14 Develop Computer Integrated Manufacturing System

Spire partnered with two lower-tier subcontractors in Phase 1. Endecon Engineering assisted with PV balance-of-systems (BOS) issues for module design in Task 1. The Automation & Robotics Research Institute (ARRI) at the University of Texas at Arlington (UTA) provided process automation support for the module lay-up system (Task 4) and the string busing system (Task 5).

## 2 TECHNICAL DISCUSSION

### 2.1 Task 1 – Design Brightfield Module and Production Line

The objective of Task 1 is to design a large area PV module and associated module production line that will minimize the total installed system cost for multi-megawatt utility-connected Brightfield PV arrays. Balance-of-system (BOS) requirements were considered early in the module design process, through a site visit to Tucson Electric Power's (TEP) PV array in Springerville, AZ, and through system analyses done by Endecon Engineering.

#### 2.1.1 Brightfield Photovoltaic Module Design

Spire Solar and Endecon engineers visited TEP's 3.5 MW PV array in August 2003. The array uses three types of modules: 45 W amorphous Si, 50 W CdTe, and 300 W EFG Si (Figure 1). TEP found that large modules minimize installation labor for mounting and making DC electrical connections. BOS costs reportedly ranged from \$3.35/W for small modules to \$0.90/W for large modules (at STC, DC). In addition, TEP installed the modules low to the ground to minimize wind loading and resulting array structure and anchoring costs. Thus a large module with a high aspect ratio (e.g., two or more) is preferred.



**Figure 1 PV sub-arrays at Tucson Electric Power in Springerville, AZ, made with 300 W (left) and 50 W (right) modules.**

Other module design factors we considered include glass size, thickness, deflection and stress under wind and snow loads, module weight, cell string busing arrangement, bus ribbon sizing, and junction box and diode designs. A survey of module materials was done to determine the maximum sizes available for glass, EVA and back sheet. Both single- and double-glass laminates were considered.

Our final design is a single-glass module, nominally 5 ft by 12 ft, made with 240 silicon solar cells, 150 mm square, connected in 10-cell strings. The strings are wired twelve in series by two in parallel. Six by-pass diodes are provided, with each diode protecting four strings, two (20 cells) in series by two in parallel. A nominal output of 3.38 W/cell (15% cell efficiency) results in a module power of 811 W. Dimensions and nominal electrical characteristics at Standard Test Conditions (25°C, 100 mW/cm<sup>2</sup>, AM1.5 Global spectrum) are provided in Table 2.

**Table 2 Nominal specifications for the Brightfield module.**

Parameter		Value
Cells in series		120
Cells in parallel		2
Glass width	mm (inch)	1575 (62.00)
Glass length	mm (inch)	3683 (145.00)
Glass weight	kg (lbs)	92 (203)
Module weight	kg (lbs)*	140 (307)
$P_{max}$	W	811
$I_{mp}$	A	14.5
$V_{mp}$	V	60.0
$I_{sc}$	A	14.5
$V_{oc}$	V	74.0

\*Includes steel support frame

The conventional method of mounting diodes in a junction box presented some serious design issues, including a complex busing arrangement in the laminate and substantial diode heat generation in the junction box, should the diodes turn on. We eliminated these problems with an alternative approach, in which the diodes are laminated with the solar cells. A Schottky chip diode was selected for its low power dissipation under forward bias and its thin profile for lamination. Copper bus ribbon with a large cross-section was selected to conduct heat away from the diodes. Diode assemblies were fabricated with different size bus ribbons and tested for temperature rise vs. forward current. The results are shown in Figure 2. A diode laminated as it would be in a module (plotted as triangles in Figure 2) operated a few degrees cooler than a diode tested in air. The slopes of the lines fit to the data are inversely proportional to the ribbon cross-section area. We used this relationship to select a bus ribbon size that limits the diode temperature to prevent damage to the diode, the solder joint, or the encapsulant.

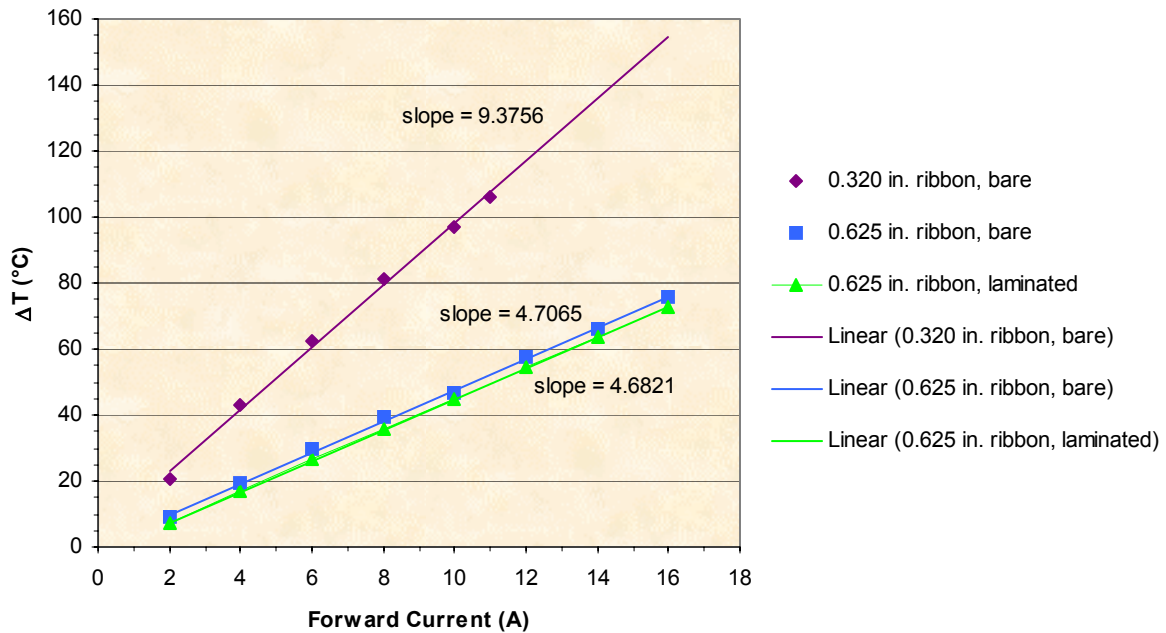


**Figure 2 Diode assembly temperature rise vs. forward current.**

The use of laminated diodes allows us to simplify the junction box, since the box is only the termination for the positive and negative outputs. We considered a central box with both outputs, as shown schematically in Figure 3. However, due to the 3.68 m length of the module, we were able to significantly reduce series resistance losses in the laminate busing and in the external cabling by using separate terminal boxes at opposite ends of the module. Only short cables and a connector are needed to connect two modules in series. The module circuit for this design is shown in Figure 4.

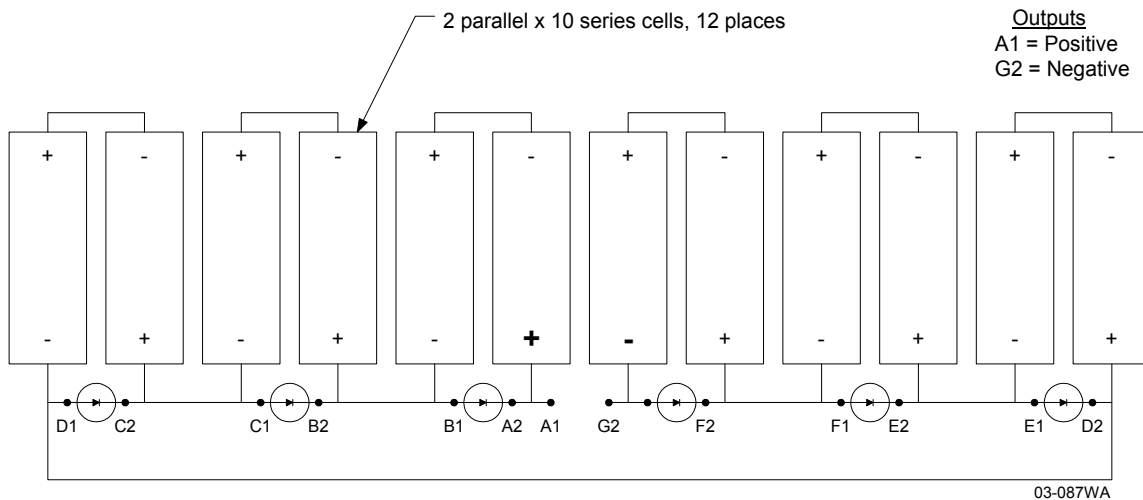


**Figure 3 Module circuit with laminated diodes and center outputs.**

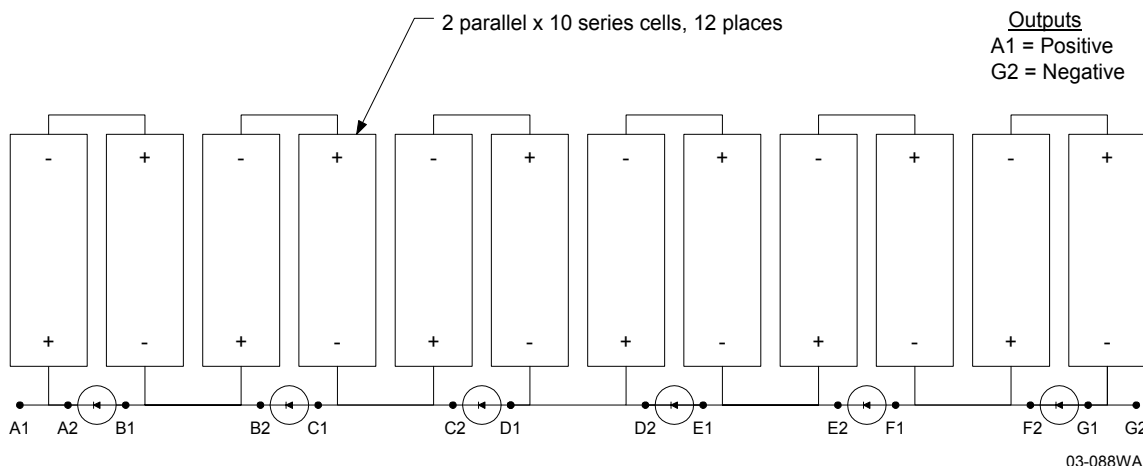


**Figure 4 Module circuit with laminated by-pass diodes and end outputs.**

Glass deflection and stress under wind and snow loads were calculated for various glass sizes and thicknesses, and for single and double glass module constructions. In place of a conventional extruded aluminum edge frame, we designed a frame from welded steel angle for mounting and mechanical support. The frame is powder coated for corrosion protection and attached to the module with a structural silicone adhesive. The steel angles are arranged so that the glass is supported at approximately 1/5<sup>th</sup> and 4/5<sup>th</sup> of the module's width. This reduces the glass span by 40% in the width direction, allowing the use of a thinner (lighter and less expensive) glass superstrate. A center support is provided at the midway point of the module's length for attaching a pair of support legs. This reduces the length of the supported span by half to allow the use of smaller steel angles. The design is shown in Figure 5.

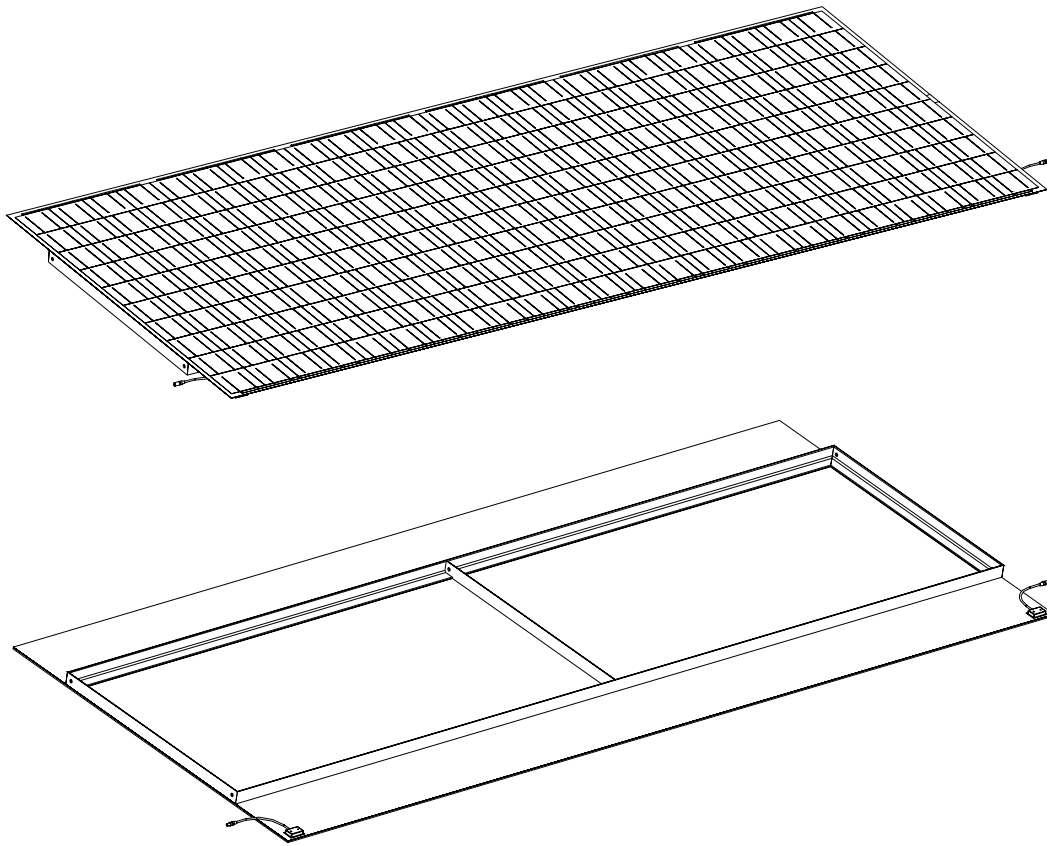


**Figure 5** Isometric views of the front (top) and back (bottom) of the 1.58 m x 3.68 m Brightfield module design, showing the cantilevered laminate and frame.

With this geometry, we are able to support the module with a single layer of 6.3 mm thick glass. Modules must be able to withstand wind and snow loads up to 5.41 kPa (113 psf), per IEC 61215 and IEEE 1262 standards. We calculated the maximum stress on a 6.3 mm thick, 1575 mm wide glass to be 44.0 MPa (6380 psi), as shown in Figure 6. This provides a comfortable factor of safety of 3.8, since the tensile strength of tempered glass is 165 MPa (24,000 psi). Note that our choice of support frame spacing balances the maximum bending stress in the center with the maximum stresses at the support angles.

A solid CAD model was created to define the steel and glass structural geometry for the module. The frame is fabricated from welded 2" x 2" x 0.19" steel angles, and includes six bolt holes for attaching legs, two on each short frame member. The model was then exported to the ANSYS® engineering software program for structural finite element analysis. The worst-case 113-psf wind and snow load was applied. The deflection of the steel frame is shown in Figure 7, with the z-scale exaggerated to show the shape of the deflection. The maximum deflection is 0.23". The total module deformation (glass and steel) is shown in Figure 8, with a maximum deflection of 0.50".

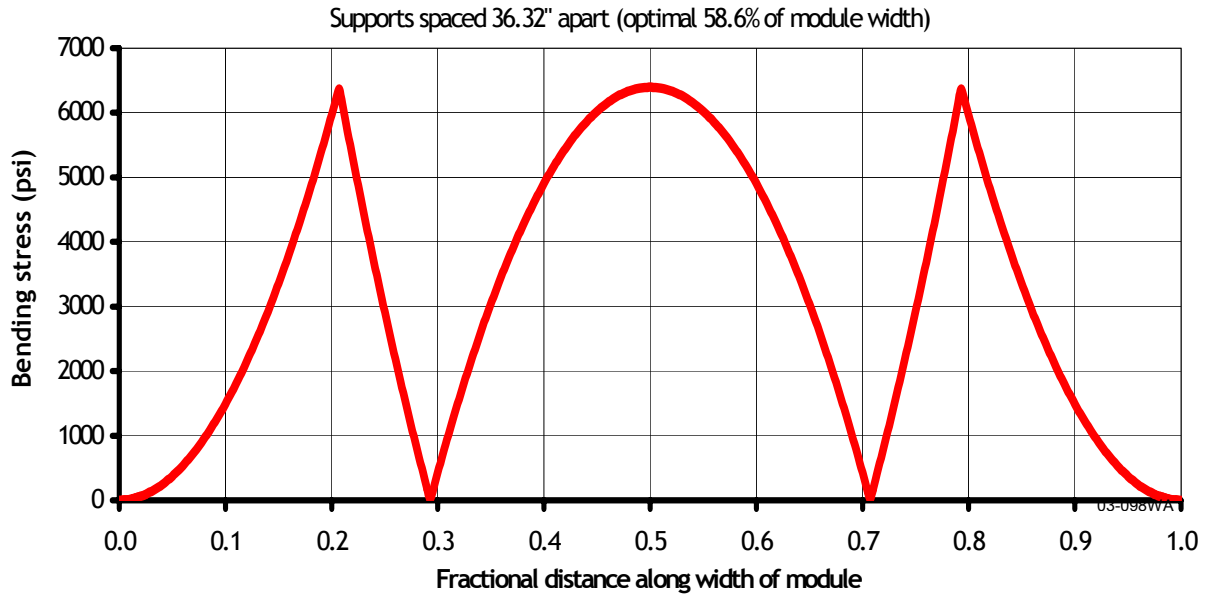


**Figure 6** Bending stress profile under maximum wind and snow load (113 psf) for a 1575 mm wide module with a 6.3 mm thick cantilevered single glass sheet.

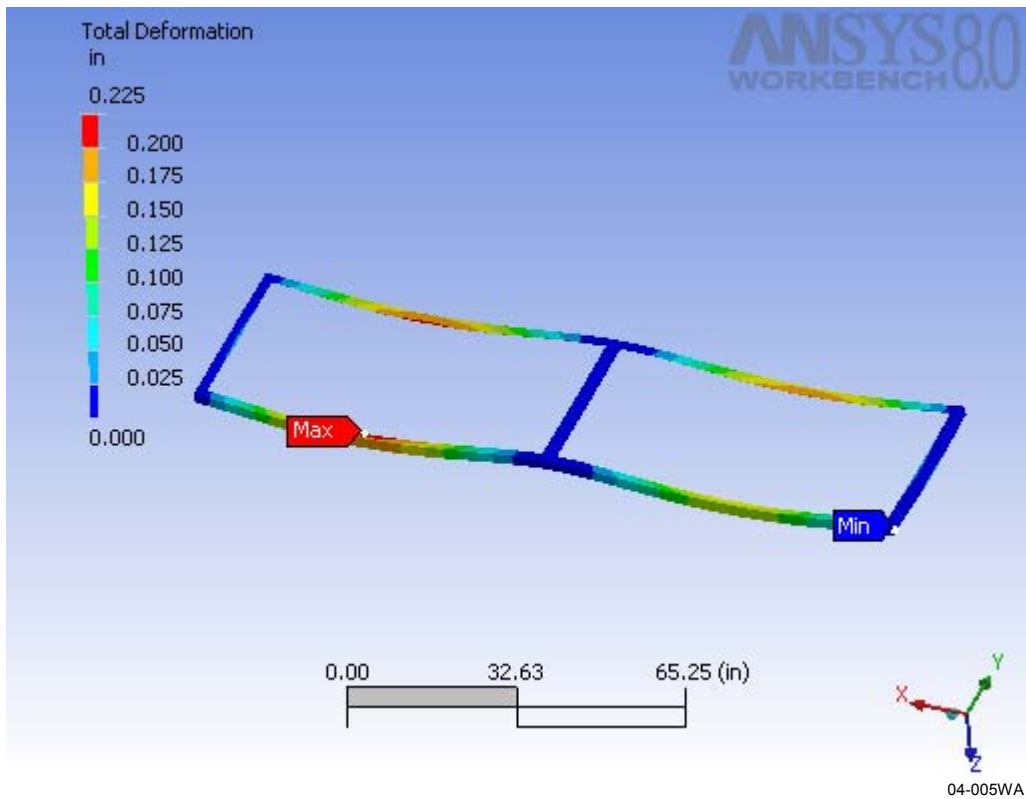


**Figure 7** Steel frame deflection under 113 psf wind and snow load.

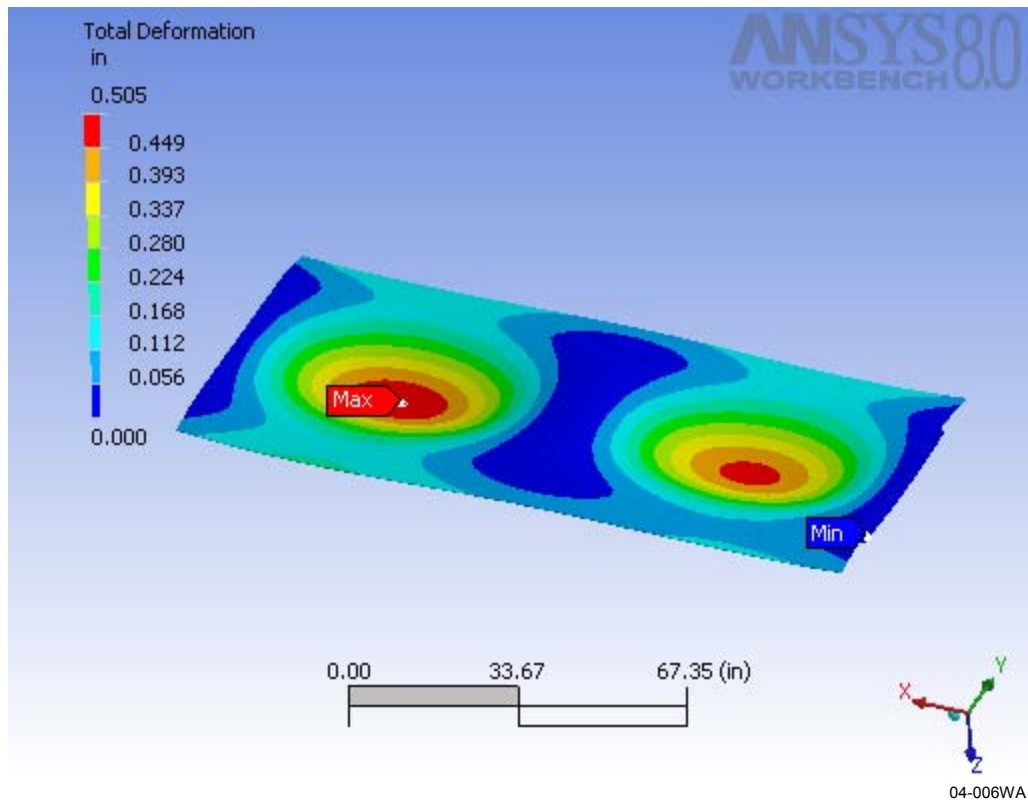


**Figure 8 Module glass and steel deflection under 113 psf wind and snow load.**

### 2.1.2 BOS Electrical Design Analysis

Behnke, Erdman & Whitaker Engineering, Inc., completed a balance of system (BOS) study for megawatt-size PV systems under Spire’s subcontract to Endecon Engineering. The study considered the elements of the electrical system from the module output to the medium voltage terminals of the step-up transformer that feeds the power line. The PV modules, AC medium voltage distribution, civil work, and construction labor costs were excluded.

The study assumed a system would be built in 1 MW blocks, each with its own medium voltage (15 to 35 kV) AC interconnection. The PV array uses our nominal 5’ x 12’ 800 W modules. Wires were sized to limit the overall voltage drop to 1%. Four cases were considered: 600 VDC monopolar (base case),  $\pm 600$  VDC bipolar, 1000 VDC monopolar, and  $\pm 1000$  VDC bipolar. Circuit diagrams, plant layouts, and bills of materials for 1 MW systems were designed and costs were determined for each of the four cases.

**600 VDC monopolar** – This is the base case for the study and the state-of-the-art for commercial, industrial, and utility scale systems. UL-listed inverters and other components (e.g., disconnects, fuses, cabling, and combiners) with third party listings are readily available. The study assumes there are ten parallel source circuits of seven series-connected modules forming a 50 kW sub-array, four sub-arrays feeding a 200-kW inverter and transformer, and five inverters and transformers per 1 MW array.

**$\pm 600$  VDC bipolar** – This design takes advantage of the 2002 NEC revision to Article 690.7, which allows bipolar circuits to be considered as two 2-wire circuits when determining maximum system voltage, so long as one wire is grounded. Thus readily available 600 V DC rated components can be used for systems with inverter inputs up to 1200 VDC. No UL-listed inverters are currently available, although suitable inverter technology exists. Non-listed inverters are suitable for “behind the fence”

utility applications. The design study assumes the use of a high power (1 MW) inverter. Listed high power inverters for non-utility applications could be available in twelve months time, with a commitment to purchase 10 MW or more per year. In this case, there are ten parallel source circuits of seven series-connected modules forming a 50 kW sub-array and twenty sub-arrays feeding a single 1000-kW inverter and transformer for each 1 MW array. Significant cost reductions were seen for this design compared to the base case due to the reduced number of inverters and transformers.

**1000 VDC monopolar** – Modules can be rated for PV systems up to 1000 VDC under UL 1703. 1000 V BOS components (except for inverters) are available for traction, mining, and crane applications, but these components are generally not UL-listed. Listed inverters are not currently available, but suitable inverter technology exists. Load-break DC disconnects with low current ratings are not readily available, making these components more expensive than the 600 V versions. Twelve parallel source circuits of twelve series-connected modules form a 100 kW sub-array. Ten sub-arrays feed a single 1000-kW inverter and transformer for each 1 MW array.

**±1000 VDC bipolar** – This design has the same advantages as the 600 V bipolar design with respect to 2-wire circuits when determining maximum system voltage ratings for components. It also has the potential, as does the 600 V bipolar design, to eliminate the inverter isolation transformer for low voltage (480 VAC) interconnections. However, it has the same drawbacks as the 1000 V monopolar design regarding the lack of available listed components. This system has the highest inverter input voltage, resulting in the lowest inverter cost. Like the 1000 V monopolar case, twelve parallel source circuits of twelve series-connected modules form a 100 kW sub-array, and ten sub-arrays feed a single 1000-kW inverter and transformer for each 1 MW array.

A cost comparison of the four BOS designs is provided in Table 3. The 600 V bipolar system has the lowest electrical BOS equipment cost, due to the availability of commercial listed components and a higher input voltage, lower cost inverter than present monopolar designs. The 1000 V bipolar system could be lower cost in the future, but currently suffers from high DC switchgear cost and availability.

**Table 3 Electrical BOS equipment cost.**

Design Case	Cost (\$/W)
600 VDC monopolar (base)	0.375
±600 VDC bipolar	0.266
1000 VDC monopolar	0.385
±1000 VDC bipolar	0.325

### 2.1.3 Production Line Definition

At 92 kg (203 lbs), the module glass is too heavy to be handled by two operators. As a result, the glass and laminates will be transported through the module production process on powered roller conveyors. A conveyor width of 68 inches was selected to handle the 62 inch wide glass. All of the assembly and test procedures are done with the module in a facedown orientation, so there is no need to turn the module over.

The module line process flow is shown in Figure 9. A preliminary production line floor plan was also designed, as shown in Figure 10.

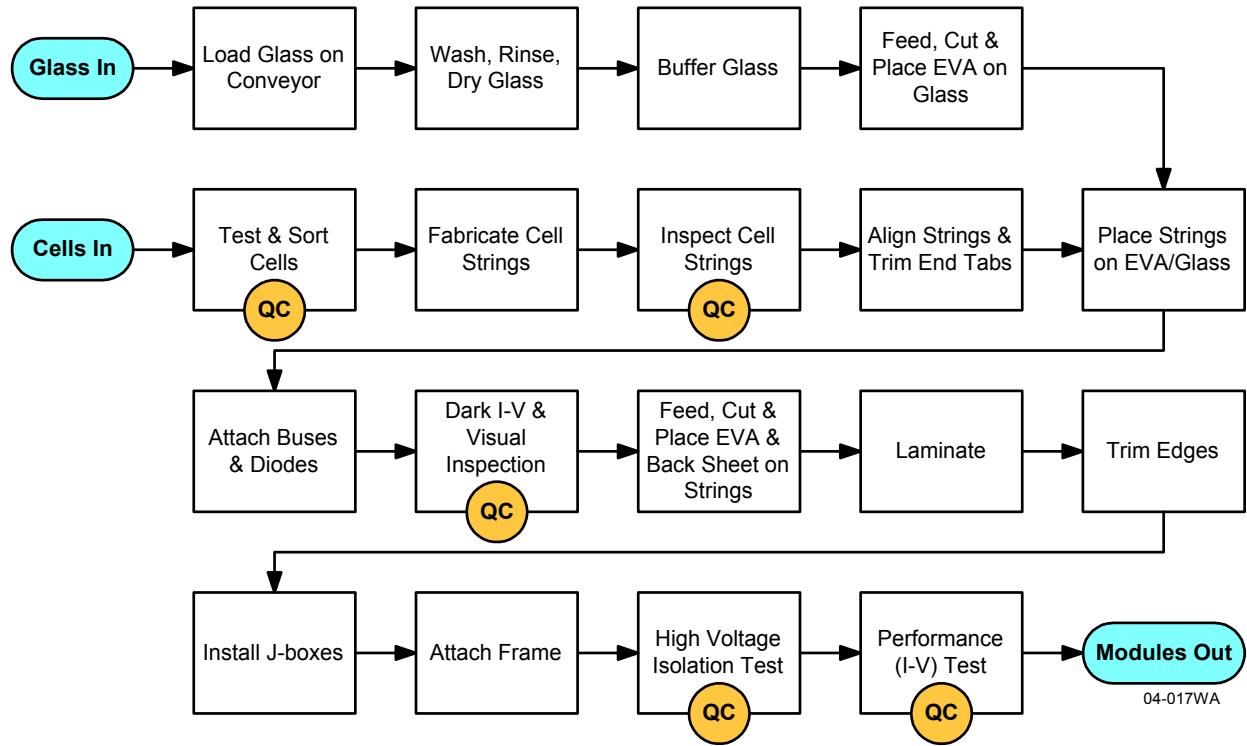


Figure 9 Brightfield module line process flow chart.

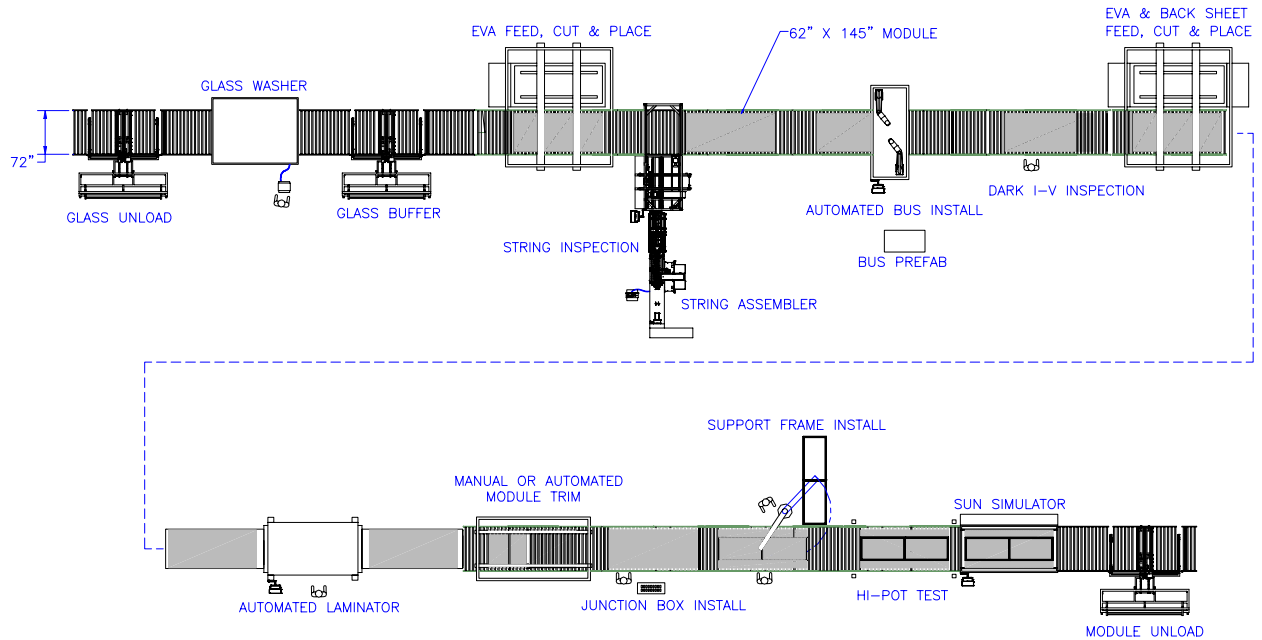
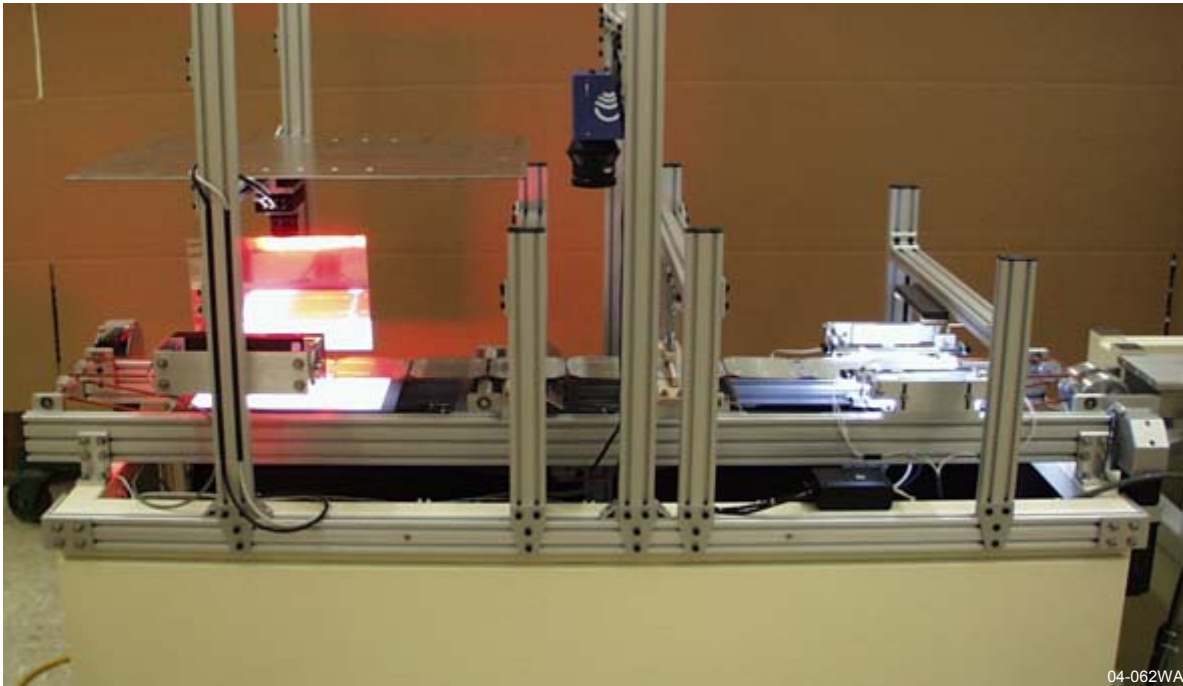


Figure 10 Preliminary module production line floor plan for the large area Brightfield module.

## 2.2 Task 2 – Develop Cell String Inspection Process

Given the large size of the Brightfield modules, each string must be carefully inspected before lamination to ensure high yields. Our efforts in this task focused on two main activities: developing machine vision techniques for identifying visible defects in cell strings, and investigating methods for detecting microcracks in solar cells that are too small to see with a vision system. This work culminated in the design, fabrication, and testing of a full-scale prototype automated string inspection system, shown in Figure 11.



**Figure 11 Automated cell string inspection system with a string of 125 mm cells.**

### 2.2.1 Visible Defect Inspections

We applied machine vision techniques to find visible defects in strings, including cell chips, separated cell cracks, cell alignment and orientation in the string, and ribbon alignment to the cell. This work began with a vision system product survey, aimed at selecting the optimum system based on capabilities, speed, cost, and ease of use. Both traditional vision systems and recently developed vision sensors were considered. After reviewing and comparing the capabilities of these systems, we selected a high-resolution DVT unit for string front and back side inspections.

Camera lenses and spacers were selected to obtain the correct field of view for front and back side inspections. Calibration plate spot patterns were designed for pixel to real world coordinate (mm or inch) translations for both front and back views. The patterns also allow corrections for lens distortion. Calibration software projects were developed for use by the operator. A Visual Basic user interface project was coded, incorporating the DVT to host PC communications protocol and display capabilities.

Polycrystalline cells present a special challenge for vision systems because they have randomly located, randomly oriented crystal grains, some of which reflect strongly under normal lighting conditions. The result is an image containing a number of bright objects of random size and location, as shown in the left image in Figure 12. These bright grains prevent the vision tools from reliably determining the locations of the cell edges and contact buses.

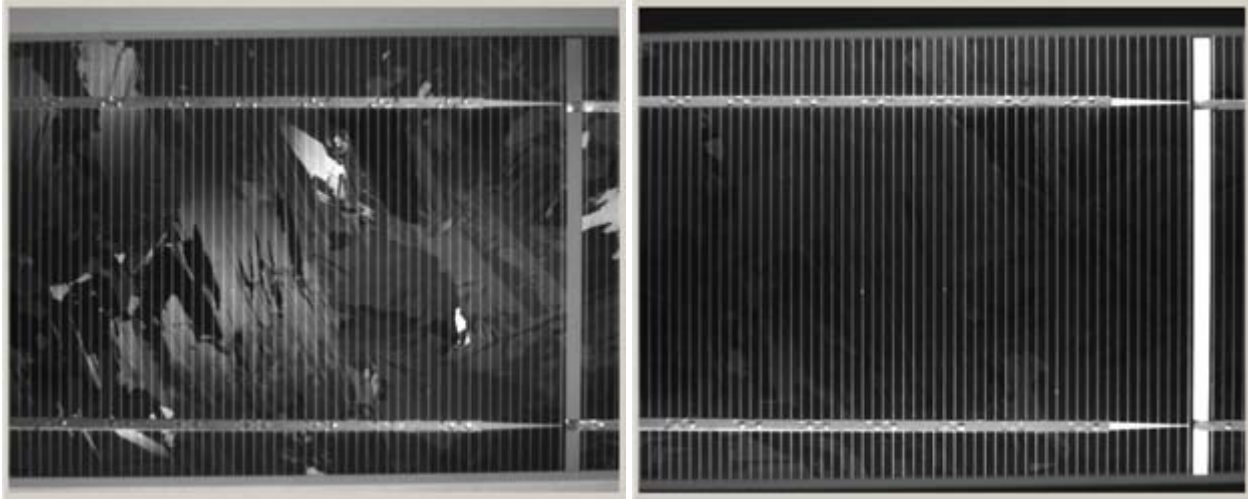


**Figure 12** Vision sensor images of a 125 mm polycrystalline silicon cell using unfiltered direct lighting (left) and using two diffuse reflectors and a spectral filter (right).

Initial lighting experiments showed that bright silicon crystal grain reflections could be eliminated by shining red LED arrays at a shallow angle onto the cell surface. However, two large, expensive LED arrays were needed to fully illuminate the cell area with sufficient brightness. After testing several alternative lighting methods, we found a lower cost approach that achieves good results. In this approach, linear fluorescent lamps shine onto diffuse reflectors on opposite sides of the cell, while a filter on the camera lens cuts out the short wavelengths responsible for most of the crystal grain reflections. The results are shown in the right image in Figure 12. The vision sensor, lamp and reflector arrangement is shown in Figure 13.

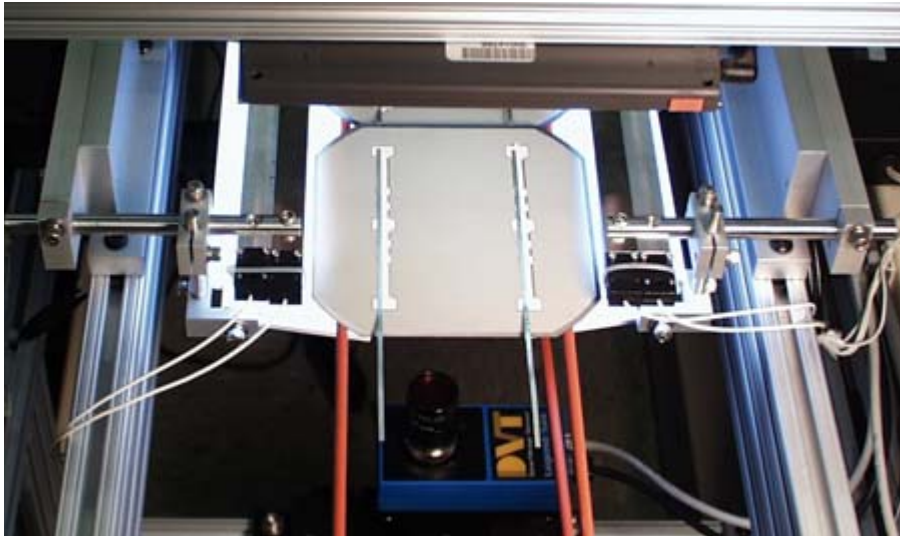
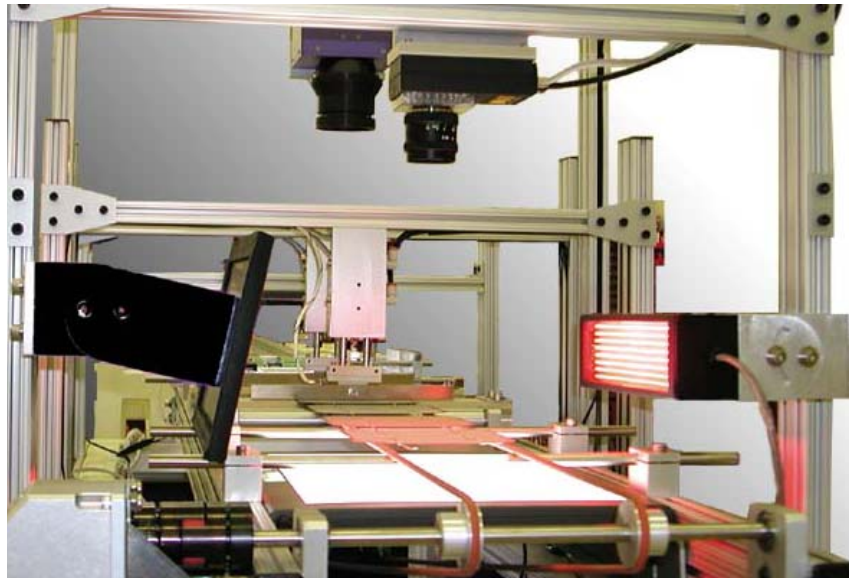


**Figure 13** Cell front side vision sensor with filter (bottom), lamps with white reflectors (left and right), and backlight (top) with a string of 125 mm cells.

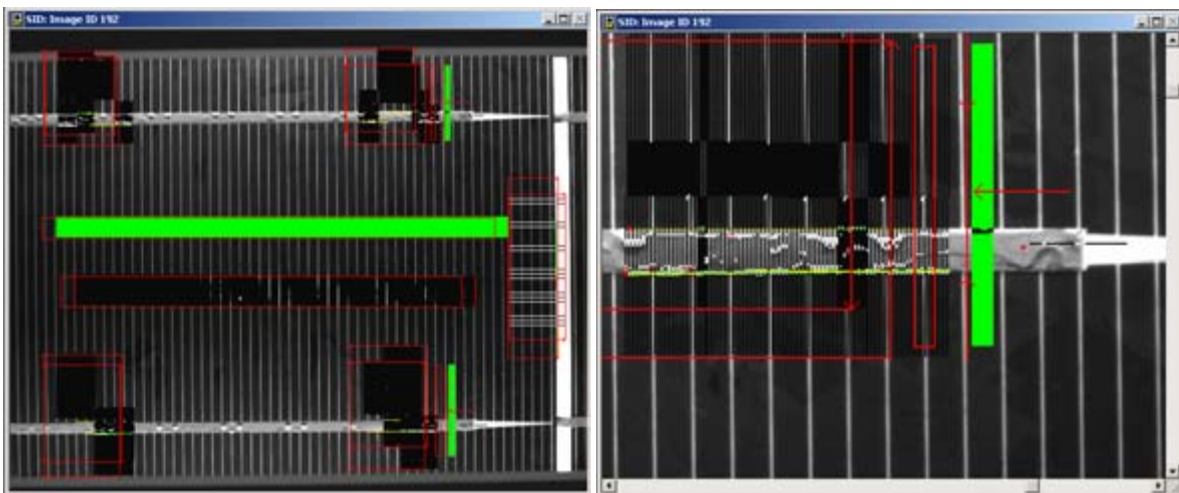
We cannot use this same lighting technique for the cell backside inspections because the lamp must be cycled on and off for each cell inspection. The lamp is turned on for cell presence and tab alignment measurements, then turned off for chip and crack detection and cell alignment measurements, which use only backlighting for maximum contrast. Fluorescent lamps are not suited for cycling, due to their long warm-up time, so we chose the red LED array approach. Since the LED array illuminates the cell surface at a shallow angle, we were able to obtain good images with only one array by installing a mirror on the opposite side of the string, as shown in Figure 14.



04-065WA

**Figure 14** Cell backside vision sensor (top), LED array (right), backlight (bottom), and mirror (left).

Once the lighting methods were determined, we developed software for visual inspections of the front and back sides of cell strings by applying image-processing tools to the vision sensor images. The tools used to inspect the string front side, shown in Figure 15, check for cell presence, cell orientation ( $0^\circ$ ,  $\pm 90^\circ$ , or  $180^\circ$ ), cell upside down, tab presence, tab alignment, and end of tab location.



04-066WA

**Figure 15** String front side vision inspection tools on a 125 mm polycrystalline Si cell. The right image is a close-up of the tools at the top right of the cell.

The tools used to inspect the string backside, with front lighting on, are shown in Figure 16. These tools inspect for cell presence, tab presence, and tab alignment. Another set of inspections done with the front light turned off is shown in Figure 17. These tools inspect for cell chips and cracks, cell-to-cell distance, and alignment of the cell's top edge to the adjacent cell's top edge.

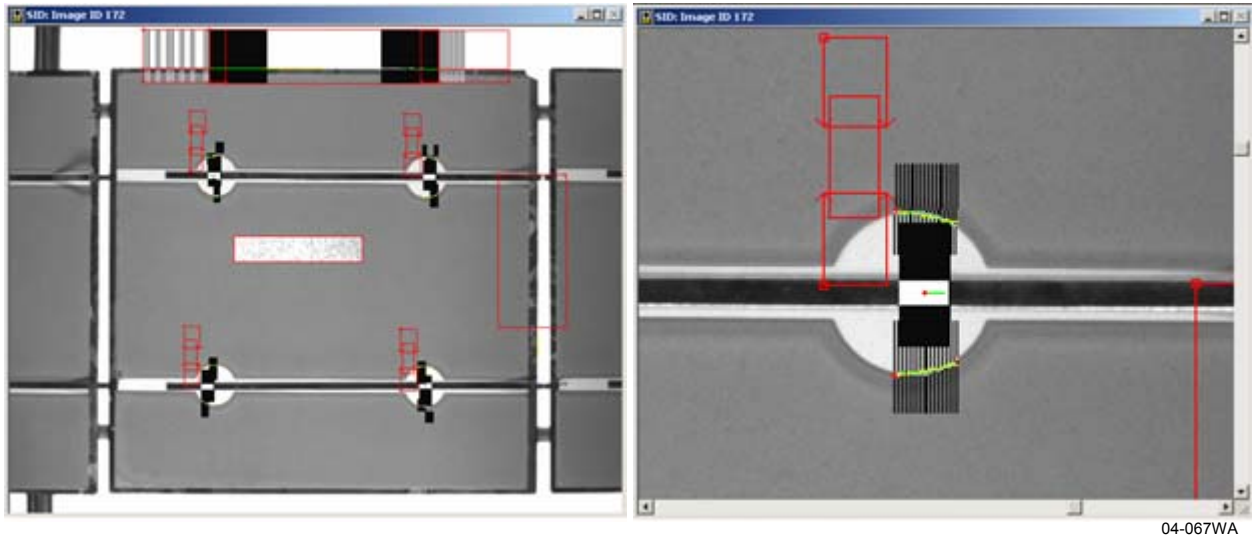


**Figure 16** String back side vision inspection tools with front lighting on a 125 mm polycrystalline Si cell. The right image is a close-up of the tools at the top right of the cell.

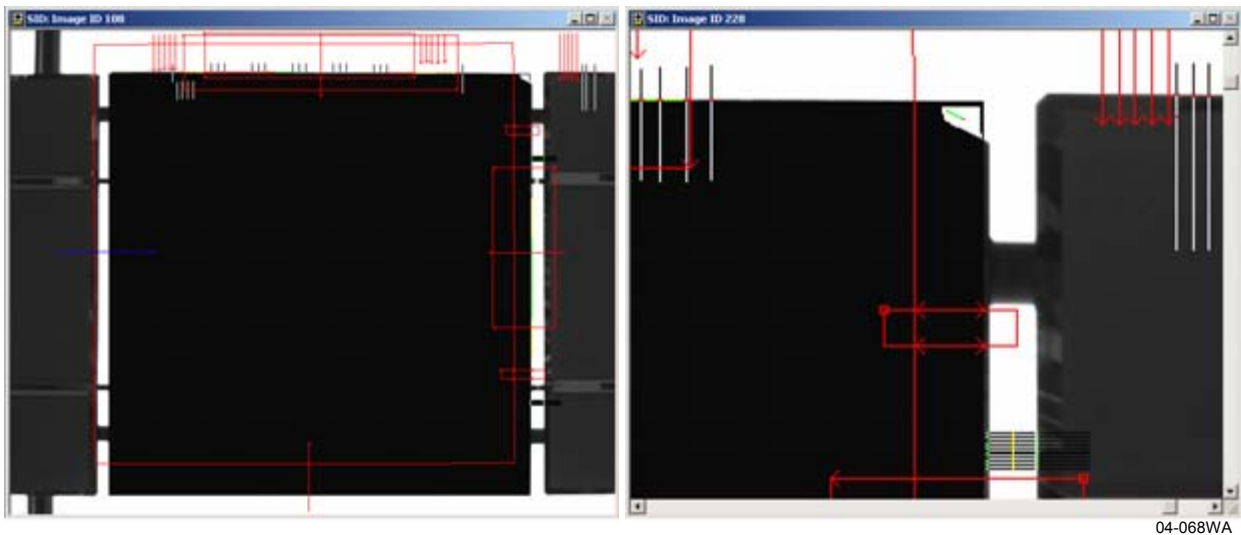


**Figure 17** String back side vision inspection tools without front lighting on a 125 mm polycrystalline Si cell. The right image is a close-up of the tools at the top right of the cell.

### 2.2.2 Microcrack Inspection

Both mono- and poly-crystalline silicon cells occasionally contain microcracks that are difficult or impossible to see with the human eye or a vision system. Module manufacturers typically use manual visual inspection to find cracked cells after cell stringing and eliminate them before module lamination. This process is labor intensive and not completely effective in finding microcracks.

Several potential methods for detecting microcracks in silicon cells were identified and considered:

**Ultrasonics** – Lassen Technologies developed a technique using a piezoelectric transducer to generate ultrasonic vibrations in a cell and detect the sonic signature of cracks. We contacted Lassen and they informed us that they are not interested in commercializing this technique.

**Radiant Heating** – A system using pulsed radiant heating (generated by a 3 kW flash tube) for crack detection is available from Thermosensorik GmbH in Germany. Cell cracks cause discontinuities in heat flow, and an infrared camera detects the temperature difference across the crack. This system was not selected because the cost is very high, and false crack detection is specified at <3%, which is too high for production.

**Thermosonics** – In this technique, ultrasonic energy causes friction heating of cracks, which an IR camera can detect as a temperature rise near the crack. Indigo Systems demonstrated their ThermoSoniX™ system at Spire on cells made from single crystal Si, cast polycrystalline Si and EFG ribbon Si. An ultrasonic horn with a blunt tip contacts the surface of a cell with a force applied by an air cylinder. A tip force of 8 to 10 lbs was applied to the cell, and 10% of full ultrasonic power was applied for 0.2 seconds. No damage was done to any of the cells during the tests.

The IR camera clearly detected microcracks approximately one second after the ultrasonic energy was applied. The system worked equally well whether the cells were face up or face down, and for gridded or solid metal back contacts. Two frames from an IR video of a test with a single crystal Si cell are shown in Figure 18. The images show the cell before and after the application of ultrasonic energy. Additional tests showed that the thermosonic system is effective at finding cracks in all three types of silicon cells.

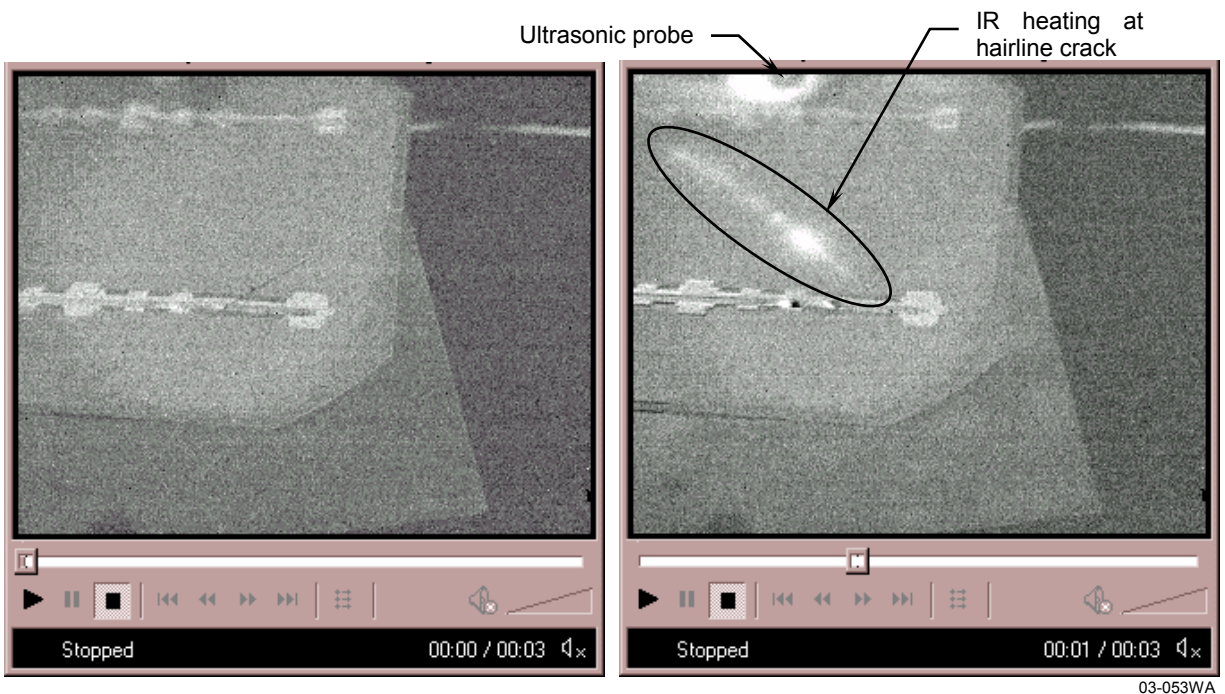


**Figure 18** IR images of the back surface of a 125 mm square single-crystal Si solar cell, before the test (left) and 1 s after the application of ultrasonic energy (right).

The ThermoSoniX system includes the software for controlling the ultrasonics and recording IR images, but it relies on a human operator to view the images and decide if a crack is present. Vision tools and analysis software are needed to automate crack detection. This approach was not pursued further because of its expense: \$95,000 for the camera, lens, ultrasonics, software, and host PC. There would be additional costs for the vision tools and crack detection software needed for full automation.

**Mechanical Flexing** – We developed an approach based on a manual cell flexing technique found to be effective for screening cells for microcracks prior to soldering. Cells are held at diagonally opposed corners and gently flexed several times. Cells with microcracks break apart easily, while good cells are not damaged. A vision sensor used to do visual inspections could then easily detect a broken cell. Since this is a low cost technique for microcrack detection, we designed, built, and evaluated a prototype flexer.

The flexing mechanism design is shown in Figure 19. The flexer has two arms mounted at 90° to each other that move up and down independently on ball slides. The arms are driven by air cylinders with low friction metal seals for smooth operation. Each arm has two rubber vacuum cups that hold a solar cell at opposite corners. The cup mount locations are adjustable for different cell sizes. A load cell on each arm measures the applied force in tension and compression.

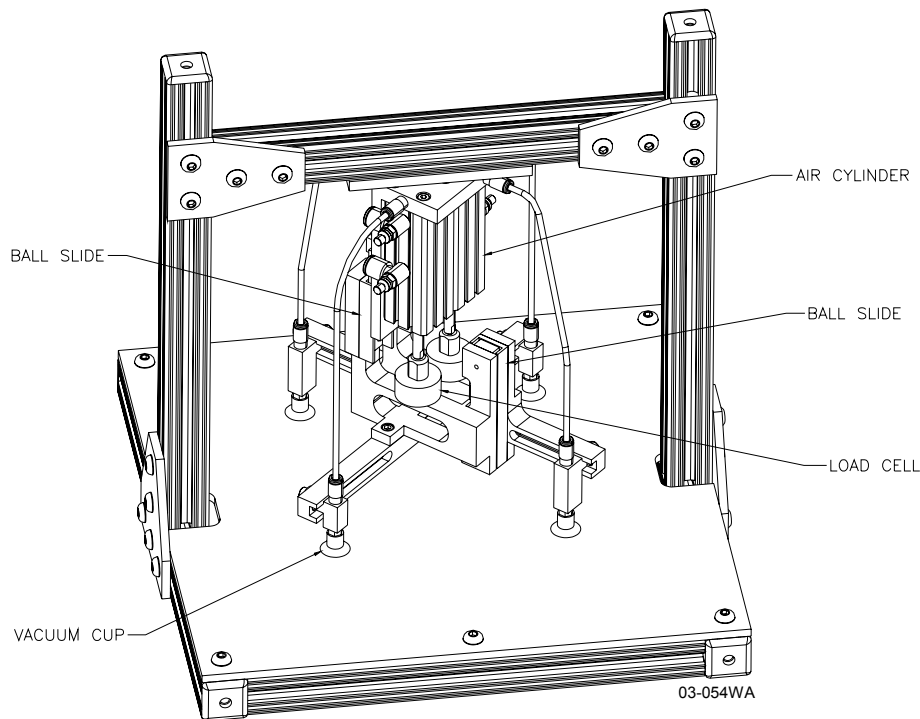
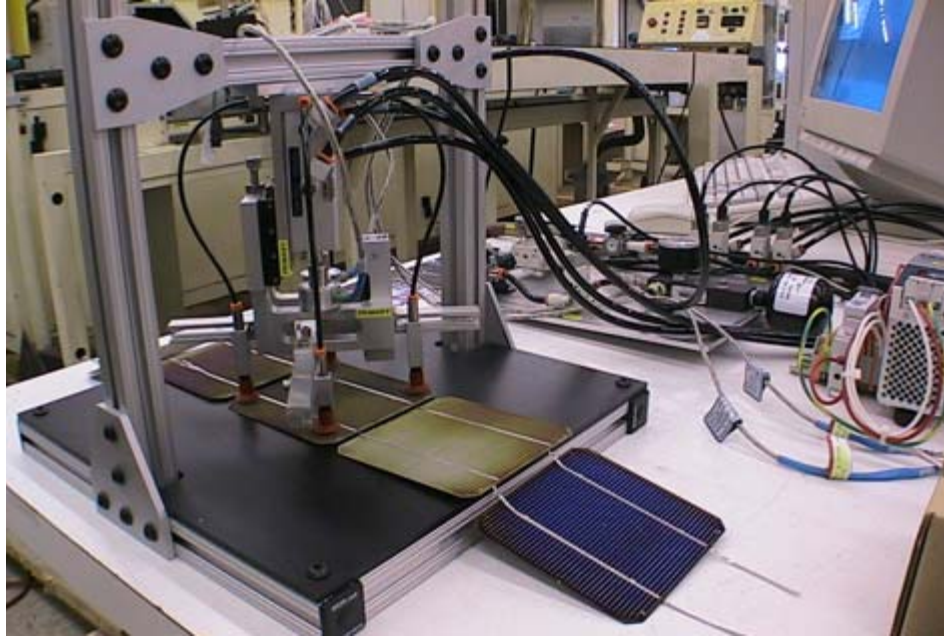


**Figure 19 Cell flexer on test stand.**

A PC with an analog and digital input/output (I/O) board controls the system automatically and acquires data from the load cells. The completed system is shown in Figure 20.

Visual Basic software was written for flexer control, data acquisition, and user interface. The software was originally written for a time-controlled cycle, in which two diagonally opposite cell corners are pulled for a fixed time and released, and then the other two corners are pulled for a fixed time and released. The user can set the pull time and the number of cycles per test.



03-068WA

**Figure 20 Prototype cell flexer on test stand with a string of Shell Solar 103 mm cells.**

A force-controlled cycle was added, in which the cell corners are pulled to a selected maximum force and released. Flexing tests were done with RWE Schott Solar EFG ribbon Si cells, 300  $\mu\text{m}$  by 100 mm square, Shell Solar monocrystalline Si cells, 300  $\mu\text{m}$  by 103 mm square, and AstroPower monocrystalline Si cells, 630  $\mu\text{m}$  by 155 mm square. Flex tests were done at two force set points, 0.5 and 1.0 lb. The software stores the peak force recorded from each load cell during each cycle in a data file. The peak force repeatability (standard deviation/average) was  $\pm 0.3\%$  or less in these tests, an excellent result given that the force is applied by air cylinders. The 10 lb load cell range and the 12 bit analog to digital converters provide a force resolution of  $10 \text{ lbs}/2^{12} = 0.0024 \text{ lbs}$ .

**Thermal Imaging with Pulse Heating** – We developed an approach that uses pulse heating, a thermal camera, and Spire-developed analysis software to identify microcracks in interconnected cells. Tests showed that this method can also identify poor soldering of interconnect leads to cells. Spire applied for a U.S. patent for this method and apparatus.

We began this development by recording infrared (IR) images while heating various types of cell strings. Microcracks appeared clearly on the IR images as thermal discontinuities across the surface of the cell, as shown in Figure 21.

The left image in Figure 21, taken before cell heating, shows a large chip missing at the upper right corner of the cell, but no cracks are evident. After three seconds of heating, the right image shows a long terminated microcrack, originating at the chip and extending diagonally down to the left. This technique has several advantages over the thermosonic method described previously. It is less expensive (no ultrasonic equipment), gentler on the cell (no ultrasonic vibrations), and the entire cell can be viewed during the test, since no probe is placed on the cell.

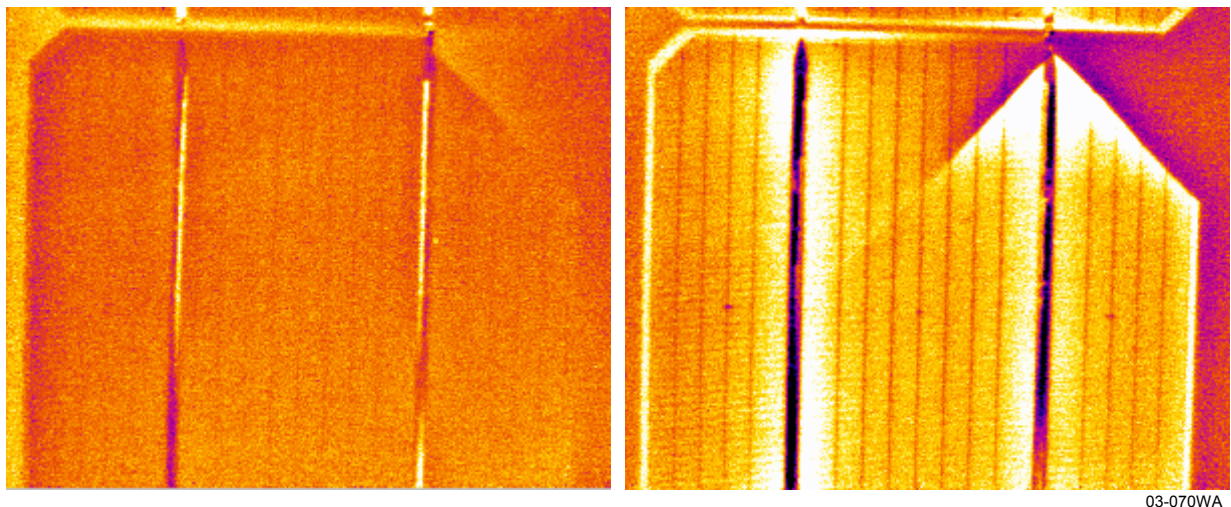


**Figure 21** IR images of a 125 mm monocrystalline Si cell with a microcrack, before (left) and after (right) 3 seconds of heating.

Our tests showed that this technique is also capable of finding sections of unsoldered interconnect ribbon on either the top or bottom cell contacts, which the thermosonic and the flexing methods cannot do. Figure 22 shows a monocrystalline Si cell with an unsoldered section of interconnect ribbon at the top left corner of the cell. Both ribbons on the near side of the cell were properly soldered, but a 25 to 30 mm length of ribbon on the far side of the cell was not soldered.

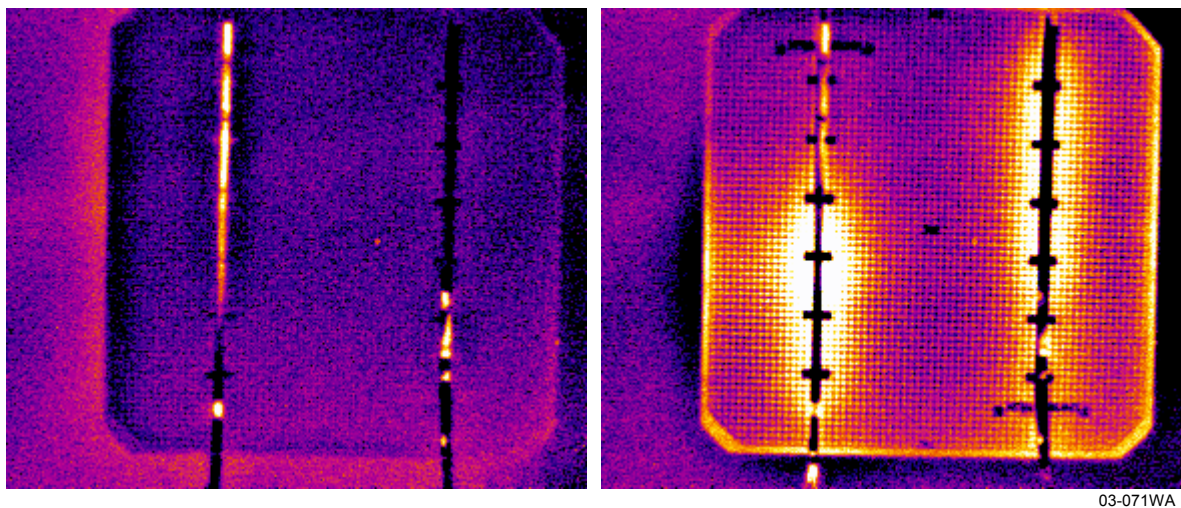


**Figure 22** IR images of 103 mm monocrystalline Si cell with a partially soldered interconnect ribbon, before (left) and after (right) 3 s of heating.

The IR camera software displays and records thermal images for viewing, but inspecting the images and deciding if there are defects were still manual processes. Therefore, we developed software that automates the inspections by applying image-processing tools to the thermal images to identify microcracks and poor ribbon soldering.

The microcrack detection method uses a blob tool configured with a gradient threshold to find thermal discontinuities when cracks are present. The left image in Figure 23 is a thermal image of a cracked monocrystalline Si cell; temperature increases as the pixel intensity varies from black to white. The right image in Figure 23 shows the blob tool inspection results for the same image. Three inspection areas

were defined on the left, center and right portions of the cell, to avoid misidentifying the contacts or interconnect ribbons as cracks. Within the inspection areas, any large change in intensity between neighboring pixels is identified and displayed in white.

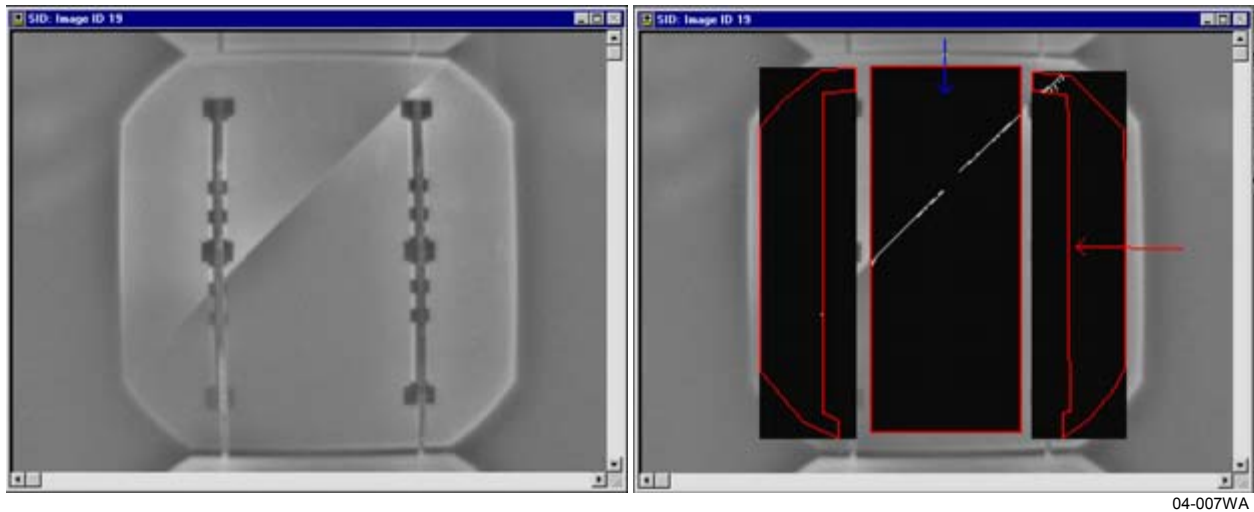


**Figure 23** Thermal image (left) and software detection (right) of a microcrack in a 125 mm monocrystalline silicon cell.

A method of detecting poor ribbon soldering was also developed. The method uses a series of intensity tools and Spire-developed scripts to measure the intensity variance ( $\sigma^2$ ) of twelve sectors of the cell. If the variance is above a selected threshold, the inspection software reports a failure. Figure 24 shows a thermal image of a cell with poor soldering in the top left quadrant and the results of the intensity tools placed on it. The sector in the top left corner and the adjacent sector to the right have low intensities that increase the variance above the failure threshold. An alternative method was also developed, where the intensity of each sector is compared to its counterpart from a trained good cell. A failure is reported if any of these comparisons exceeds a selected threshold.

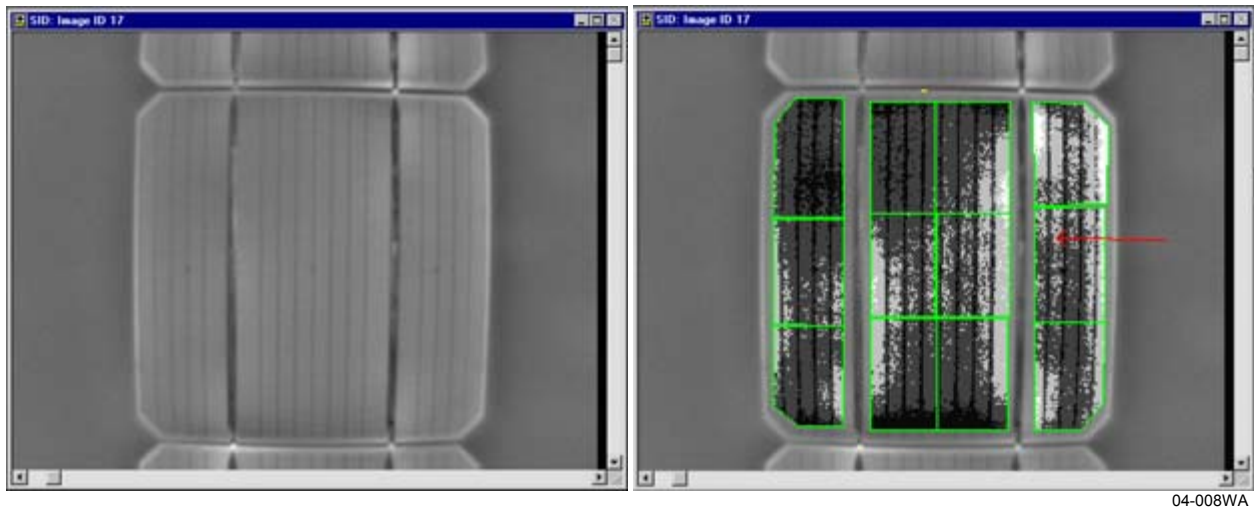


**Figure 24** Thermal image (left) and soldering inspection results (right) for a 125 mm monocrystalline silicon cell.

### 2.2.3 String Inspection System Integration

A prototype automated string inspection system was designed, fabricated, and tested. The system can be operated as a stand-alone unit or integrated with a cell string fabrication tool, such as the SPI-ASSEMBLER 5000, as shown in Figure 25.

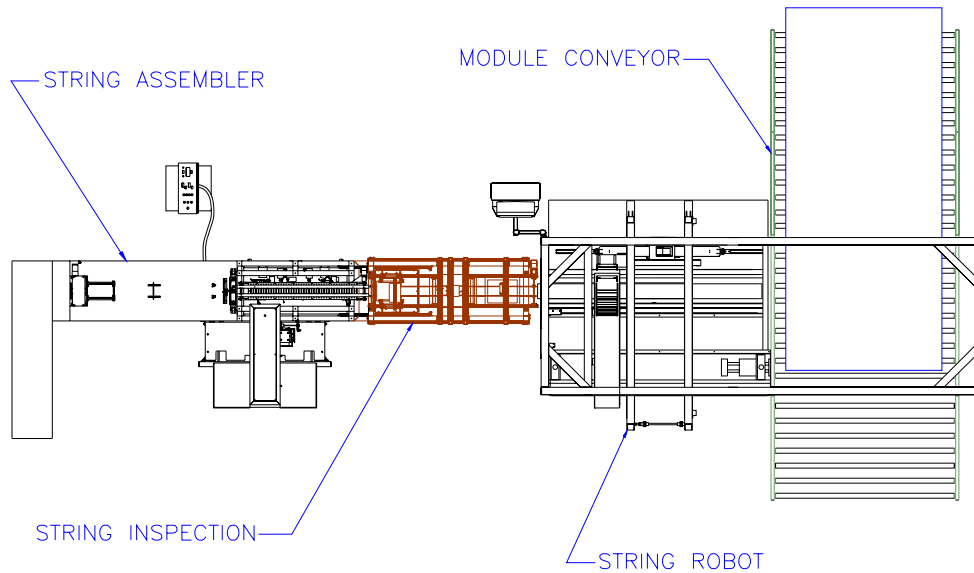
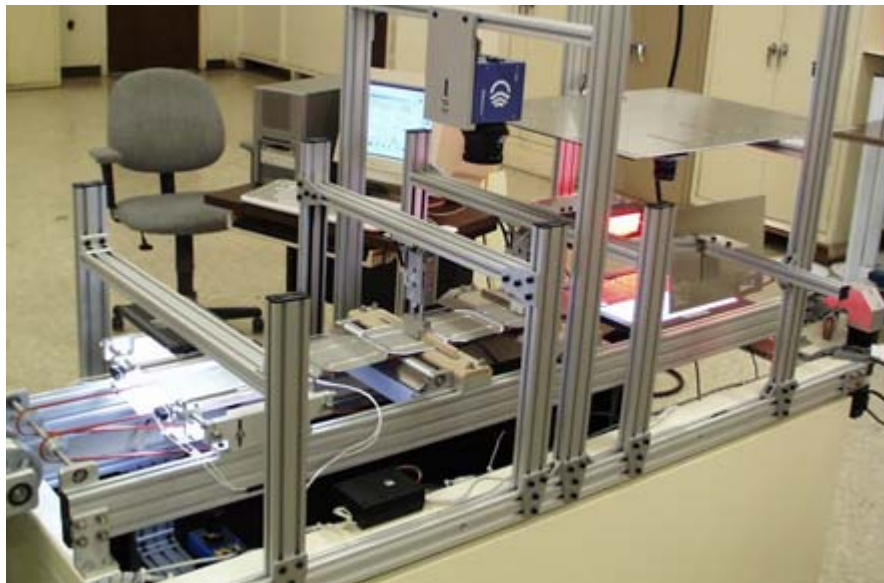


**Figure 25 String inspection system integrated with string and module assembly (plan view).**

An o-ring conveyor provides string transport with maximum visibility for inspecting both sides of the string. The conveyor and the component mounts for cameras, front lighting, backlighting, and probes are adjustable for inspecting cell sizes up to 200 mm square. A PC running Microsoft Windows 2000 controls the inspection system and acquires data from the vision sensors and thermal camera through Ethernet and USB connections. The completed system is shown in Figure 26.



04-043WA

**Figure 26 Cell string inspection system with a string of 125 mm cells.**

Visual Basic software was developed for system operation, diagnostics, calibration, and cell string inspections. A complete graphical user interface (GUI) was also developed. The main operating window, shown in Figure 27, includes operator controls, tab access to all three camera views, string and defect counters, an animated view of string location on the conveyor, and drop-down menus for all software functions.

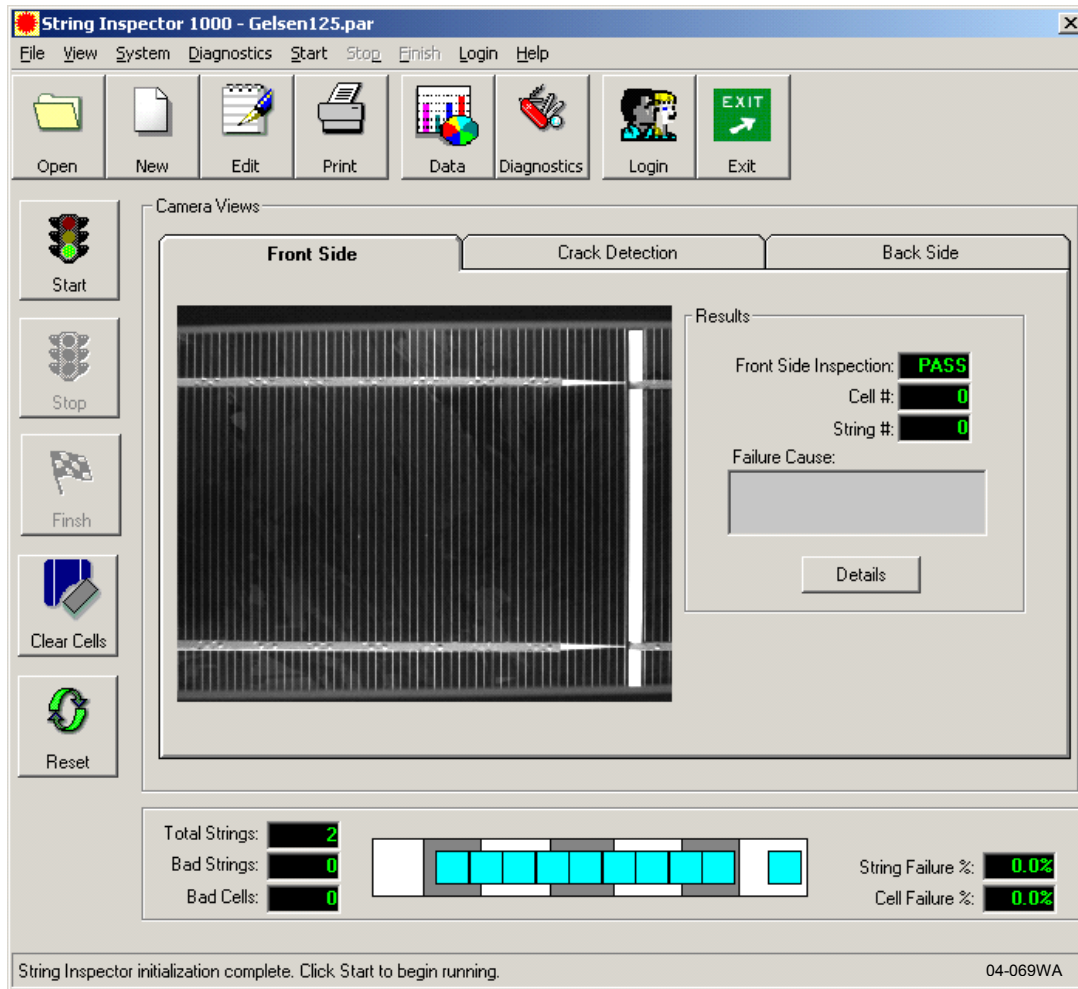
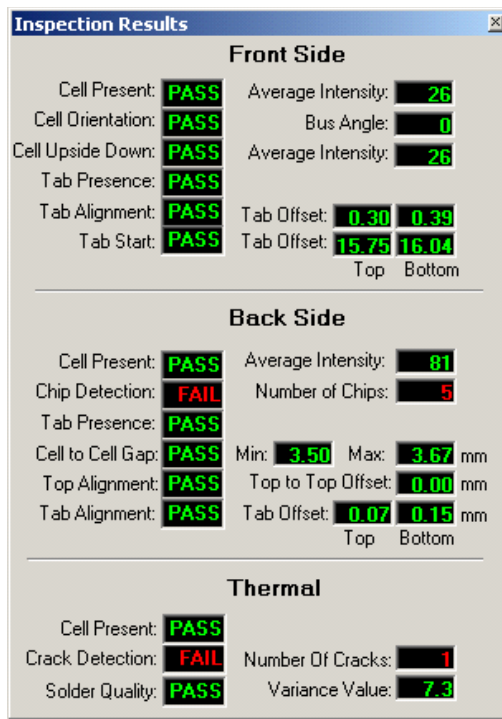


**Figure 27 Inspection system main window with cell front side camera view selected.**

Figure 28 shows the inspection results window, which displays the pass/fail results of the six front side visual inspections, six back side visual inspections, and three thermal inspections. Measured inspection data is also displayed, including average pixel intensity, cell angle, tab locations, number of chips, cell-to-cell gap, cell top edge alignment, number of cracks, and thermal intensity variance.

The results of all inspections are logged in a database file. String inspection failure reports can be generated for each batch of strings. The number of failures can be plotted by inspection category in a bar chart. Trend analyses can be done on the inspection data to monitor the measured values over time.



04-073WA

Figure 28 Inspection results window.

## 2.3 Task 3 – Develop Advanced Lamination Process

### 2.3.1 Faster Curing Encapsulant

We evaluated a new faster-curing ethylene vinyl acetate (EVA) based encapsulant, type 15420P from Specialized Technology Resources (STR), to see if we could improve the productivity of our lamination process. A lamination test matrix was completed under a range of process conditions (temperature, pump time, press time) with a SPI-LAMINATOR™ 480. The laminates were evaluated with gel tests, peel strength tests, and visual inspections for defects such as bubbles or wrinkles in the back sheet. The total process time, including time for loading and unloading, was reduced from 14.0 to 8.5 minutes, while maintaining good adhesion and high EVA gel contents (>80%).

Two laminates produced using the new process were shipped to NREL in April 2004. Each laminate is 52.5 cm x 118.2 cm and contains thirty-six 125 mm pseudo-square monocrystalline silicon solar cells from BP Solar. The laminates were fabricated in the module production facility at Spire Solar Chicago.

One of these laminates (serial no. 2813, shown in Figure 29) was made using a process we developed earlier on test laminates made with reject cell strings. This process has a 2.5-minute pump time and a 4-minute press time at 175 °C. Attempts to make an additional laminate with this process failed, due to the presence of bubbles in the encapsulant after lamination. While these laminates are the same size as the test laminates made previously, they contain more cells and bus ribbons, which are soldered at the ends of the strings. We solved the bubble problem by increasing the pump time by 30 s, which indicates that the additional components, or perhaps added volatiles from the flux residue in the additional solder joints, require more time for complete outgassing. Therefore, the second laminate we delivered (serial no. 2832) was made with a 3-minute pump time and a 4-minute press time.

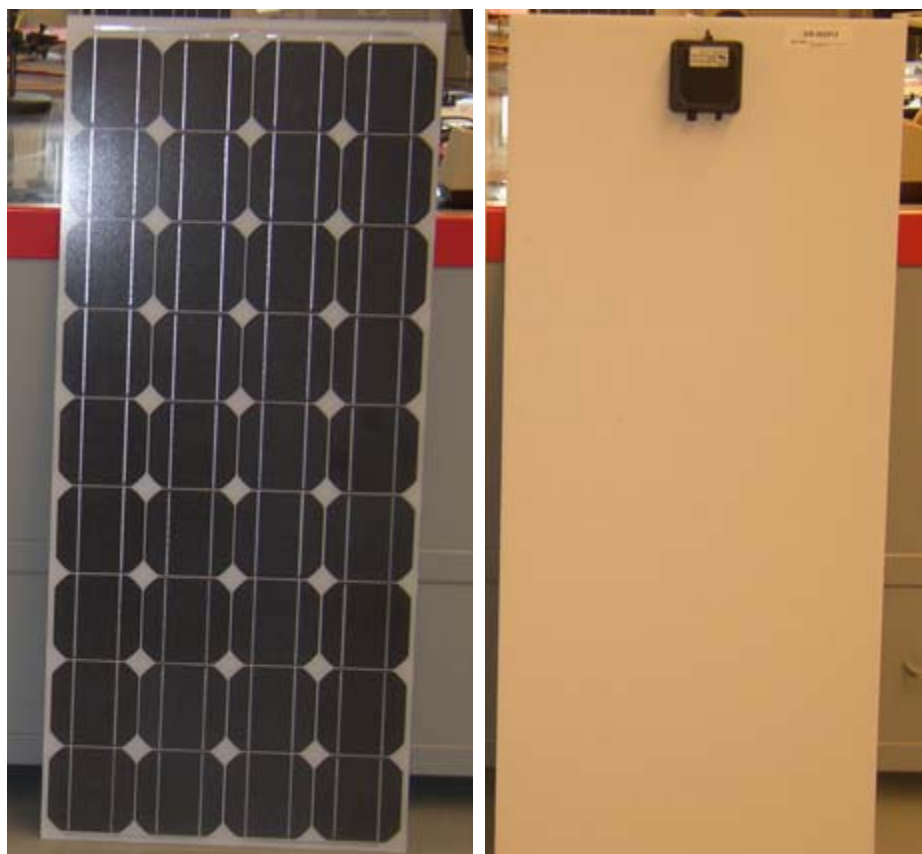


**Figure 29 Module laminate made with faster-curing EVA (serial no. 2813).**

The electrical performance of the two laminates was measured at Standard Test Conditions (STC, 100 mW/cm<sup>2</sup>, 25 °C, Air Mass 1.5 Global spectrum) with a SPI-SUN SIMULATOR™ 350i. The results are provided in Table 4.

**Table 4 Laminate electrical performance at STC. Laminate area = 6205.5 cm<sup>2</sup>.**

Serial No.	V <sub>OC</sub> (V)	I <sub>SC</sub> (A)	P <sub>MAX</sub> (W)	FF (%)	V <sub>MP</sub> (V)	I <sub>MP</sub> (A)	η <sub>MOD</sub> (%)
2813	21.83	4.811	77.52	73.8	17.71	4.378	12.5
2832	21.68	4.771	76.53	74.0	17.53	4.366	12.3

Our standard lamination cycle with STR formulation 15295P/UF EVA is processed at 155 °C with a 5.5-minute pump time and a 7-minute press time, for a total of 12.5 minutes. The new faster-curing 15420P/UF EVA, with a 3-minute pump and a 4-minute press, saves 5.5 minutes per run. Since both processes require roughly 1.5 minutes for cover opening, loading, and cover closing, the total cycle time has been reduced from 14 minutes to 8.5 minutes. As a result, production through the laminator increases from 4.3 to 7.1 runs/hour.

### 2.3.2 Laminator Cold Trap

We investigated methods for reducing laminator maintenance costs and equipment downtime caused by contamination of the vacuum pump oil by volatiles released from the EVA encapsulant. The volatiles increase the oil viscosity to the point where the oil must be changed frequently (typically after 40 hours

of operation) to prevent pump damage. We considered replacing the standard oil-filled rotary vane pump with a dry pump, but we found that the costs of dry vacuum pumps with suitable flow rates are extremely high. We then decided to investigate the use of a cold trap for condensing volatiles from the EVA before they reach the vacuum pump and contaminate the oil.

A cold trap assembly was designed, fabricated, and installed in the vacuum line between the laminator process chamber and the vacuum pump, as shown in Figure 30. The main components are a water-cooled stainless steel cold trap and a chiller for circulating coolant in a closed loop. The chiller is rated for temperatures down to  $-25\text{ }^{\circ}\text{C}$ , so a 50/50 solution of ethylene glycol and water is used to prevent the coolant from freezing. The assembly was installed and is under evaluation on a laminator in the module production facility at Spire Solar Chicago (SSC).



**Figure 30 Cold trap and chiller installed on laminator vacuum system.**

Vacuum system pump down tests were done with and without the cold trap to see if the trap reduces the laminator pumping speed. The trap was at room temperature during these tests. Figure 31 shows the pressure in the laminator process chamber during pump down, starting from a fully vented (760 Torr) condition. The trap introduced a slight restriction during the initial high-flow portion of the pump down, resulting in a higher chamber pressure (191 vs. 85 Torr) after 10 s of pumping. However, the chamber pressure was nearly identical (1.01 vs. 0.96 Torr) after 30 s of pumping and beyond. Since typical lamination process pump times range from 3 to 5 minutes, the cold trap is not expected to have a negative impact on the lamination process.

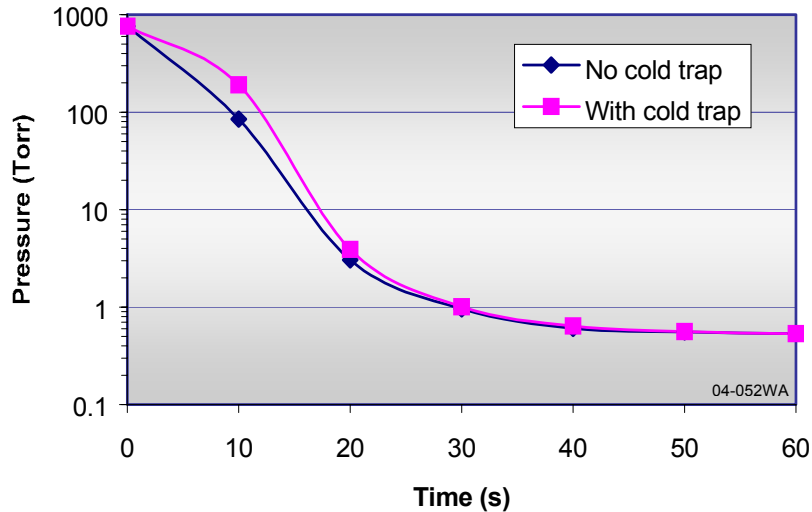


**Figure 31 Laminator process chamber pump down with and without a cold trap.**

### 2.3.3 Laminator Heater Thermal Compound

Module laminators use heated platens to melt and cure the EVA encapsulant. Since the process is done in a vacuum, Spire laminators use a thermal compound to ensure good thermal conduction between the heaters and the platen. The compound is a paste that, after some years of use, can migrate away from the heater-platen interface, due to repetitive thermal cycling. If migration occurs, the temperature uniformity of the platen can degrade with time, and the platen must be rebuilt, which involves disassembly, cleaning, application of new compound, and reassembly.

We are investigating a solid thermally conductive material that may eliminate the labor and downtime required to rebuild the platen. We compared several different materials and selected a graphite composite sheet, 0.13 mm (0.005 inch) thick, with a thermal conductivity of 5 W/mK and a temperature rating of 300 °C.

We designed and fabricated a single-heater section of a laminator platen for bench tests. Our objective is to evaluate the durability of the conductive material to withstand thermal stress from the heater and mechanical stress from thermal cycling. A heater and a water cooling line were clamped to the platen with the solid conductive material in place of thermal compound. The platen is instrumented with a control thermocouple and an over-temperature protection thermocouple on the bottom surface of the platen, and six monitor thermocouples on the top surface. Controls were designed and assembled to allow automatic thermal cycling. Software was written for operation and data acquisition. The graphical user interface (GUI) is shown in Figure 32.

The test platen was disassembled to inspect the condition of the graphite composite material on May 13, 2004, after the platen assembly had completed 823 thermal cycles. Most of the cycles were between 100 °C and 160 °C. No damage or other visible change was apparent in the graphite material at the heater-platen interface or at the cooling line-platen interface. The platen was reassembled and the temperature cycling tests are continuing at temperatures up to 180 °C. As of June 2, an additional 243 cycles were completed.

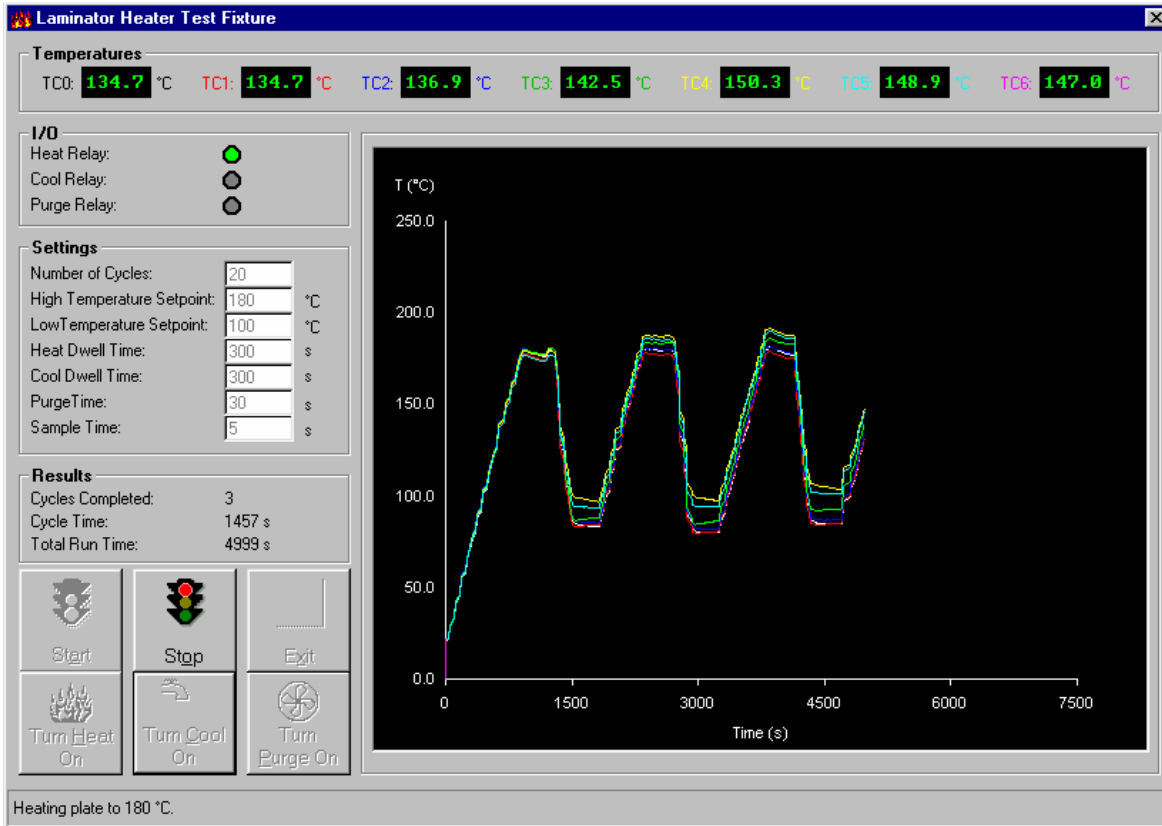


Figure 32 Laminator heater test fixture control program GUI.

## 2.4 Task 4 – Design Module Lay-up System

Concepts were developed for automating the placement of large sheets of EVA and back sheet material for module assembly prior to lamination. The Automation & Robotics Research Institute (ARRI) conducted a design for automation (DFA) analysis of the busing lay-up and back sheet feedthrough for connecting the output buses to the junction box. Most current production techniques are designed for manual assembly, and require multiple folds or splices of bus bar ribbons and the placement of insulating material to prevent shorting the buses to the cells. We devised an approach that uses a single vertical bend in the bus bar at each end of the module, a step that is easily automated and allows vertical placement of pre-slit sheet materials.

Due to the size of our large area module, careful consideration was given to automating the placement of the sheet materials. Commercial sheeters are available for dispensing materials from rolls and cutting them to length. Three different methods were considered for transferring the cut sheets onto the module: stacking on a tray followed by pick-and-place operations; winding on a tube followed by unrolling onto the module; and direct dispensing from the sheeter onto the module.

### 2.4.1 Stacking on a Tray

In this process, a sheeter makes an aligned stack on a tray for each material lay-up step. The trays are transported on conveyors or carts to two large pick-and-place machines that transfer the materials to the module. The first pick-and-place transfers EVA onto glass, while the second transfers EVA and back sheet over the cell strings, as shown in Figure 33.

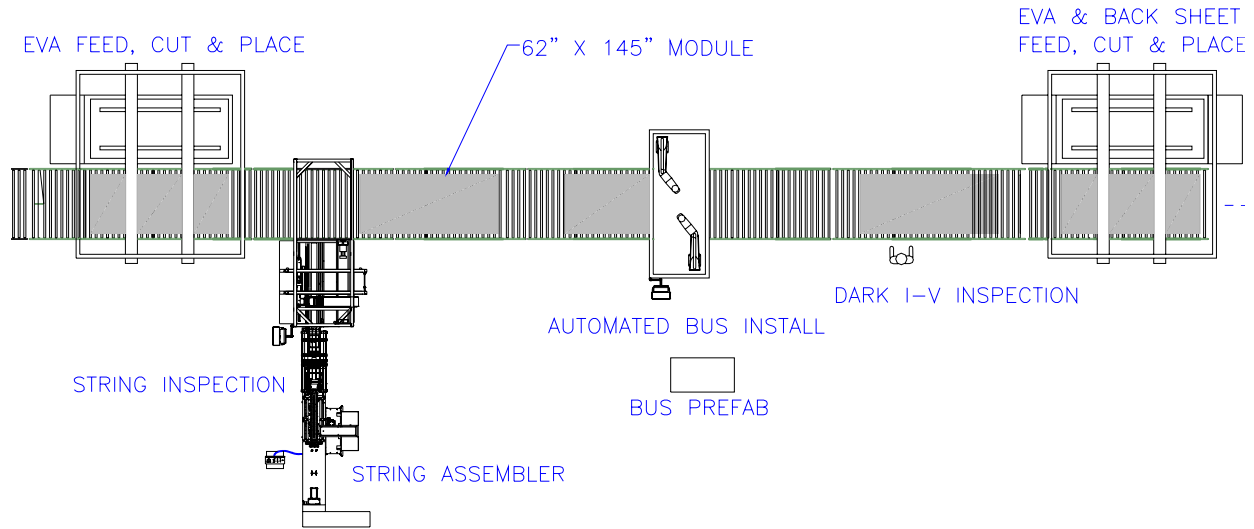


**Figure 33 Pick-and-place option for material lay-up in module production.**

ARRI designed and fabricated a prototype full-scale (5 ft x 12 ft) vacuum end effector to demonstrate a pick-and-place stack transfer process for large area sheets. Figure 34 shows a 5 ft x 12 ft sheet of Tedlar being lifted by the vacuum end effector. Miniature needle grippers and non-contact venturi air grippers were investigated, but found to offer no cost advantage relative to the standard vacuum cup method.



**Figure 34 Tedlar sheet (5' x 12') lifted by a vacuum end effector.**

A prototype mechanism was developed for opening a slit in the EVA and the Tedlar to allow the output bus leads to feed through. This allows the sheet materials to be lowered onto the module in a single vertical motion. The mechanism, mounted at the corner of the sheet end effector, consists of a cleated 1-inch diameter vacuum cup attached to the end of a small pneumatic cylinder. The cylinder is positioned so that when it is retracted, the bus lead slit is almost tangent (2 mm offset) to the attached vacuum cup. One of the stationary vacuum cups is located on the opposite side of the slit. As the sheet is lowered toward the vertical part of the bus lead, the pneumatic cylinder extends and the vacuum cup opens the slit to allow clearance for the lead (Figure 35).

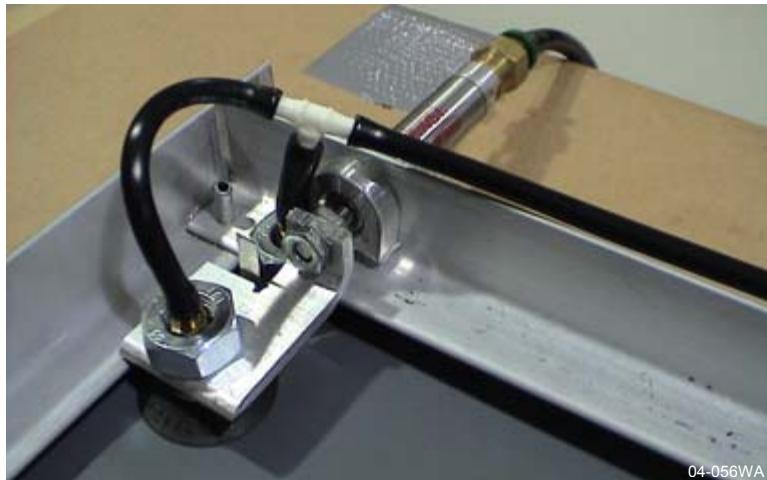


**Figure 35** End effector with cylinder actuated, cup extended, and bus lead fed through slit.

#### **2.4.2 Winding onto a Tube**

In this approach, the sheeter has a material rewind system for winding cut sheets on tubes. The tubes are transported to two simple lay-up stations where the material is unrolled onto the module. Tracks on both sides of a module conveyor guide the tube wound with sheet material across the module, powered by gravity. This approach replaces the large pick-and-place mechanisms with simpler and much smaller track structures. ARRI successfully prototyped this unrolling process for large sheets of material, as shown in Figure 36. While this method is the most space efficient and least costly of the three methods we considered, only one sheet of material is wound on each roll, and the roll handling is manual, so this approach makes sense when complete automation is not required.



**Figure 36** Prototype sheet unroller.

#### **2.4.3 Direct Dispensing onto the Module**

This approach provides full automation using a sheeter with an output conveyor belt for cut material, mounted over the module conveyor. The sheeter dispenses the material directly onto the module, as the module passes below. Sensors and servomotors synchronize the material with the module. Two sheeters are required, one for dispensing EVA onto glass, and one for dispensing EVA and Tedlar back sheet over the cells strings.

Rosenthal Manufacturing produces sheeters of this type, which they call Cover Sheet Applicators (CSA). A standard CSA is shown in Figure 37. The CSA can dispense a single layer of dimensionally stable material, such as Tedlar, with a tolerance of  $\pm 0.8$  mm ( $\pm 1/32$  inch), while EVA sheet, due to its elastomeric nature, can be dispensed with a tolerance of  $\pm 4.8$  mm ( $\pm 3/16$  inch).

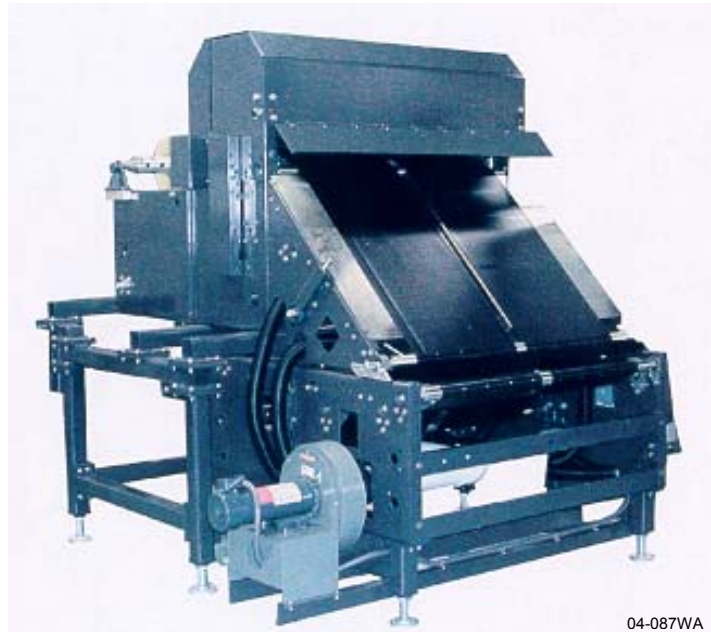


**Figure 37 Cover Sheet Applicator for feeding, cutting and dispensing sheet materials.**

We are working with Rosenthal to define a customized CSA that can handle the material requirements of our Brightfield module. Tests are underway to determine if the CSA will be capable of feeding and cutting to length two different sheet materials (EVA and Tedlar back sheet) simultaneously, without excessive slipping of the top layer. ARRI sent rolls of Tedlar (50 ft  $\times$  60 inch) and EVA (50 ft  $\times$  52 inch) to Rosenthal for these tests. If the tests are not successful, a second output conveyor belt will be added for dispensing the EVA and Tedlar separately.

An in-line die set will be installed to punch a rectangular cutout at two corners of the sheet for feeding bus leads through to the junction boxes. The CSA will also be able to handle a single layer of material, with the die set disabled, to demonstrate the lay-up of the first layer of EVA onto the glass sheet. A CSA sheeter configured for EVA dispensing is shown in Figure 38.

The Cover Sheet Applicator is preferred over the sheeter-stacker for the sheeting and lay-up tasks for several reasons. It eliminates the need for two 5 ft  $\times$  12 ft buffer stacks and two 5 ft  $\times$  12 ft pick-and-place units, greatly reducing the floor space requirements. Also, the footprint of the CSA machine is smaller than that of the sheeter-stacker system. The CSA eliminates the need to transport stacks of sheet material from the sheeter-stacker to the two pick-and-place machines. The CSA has no drawbacks in terms of cycle time or placement precision relative to the stacking system.

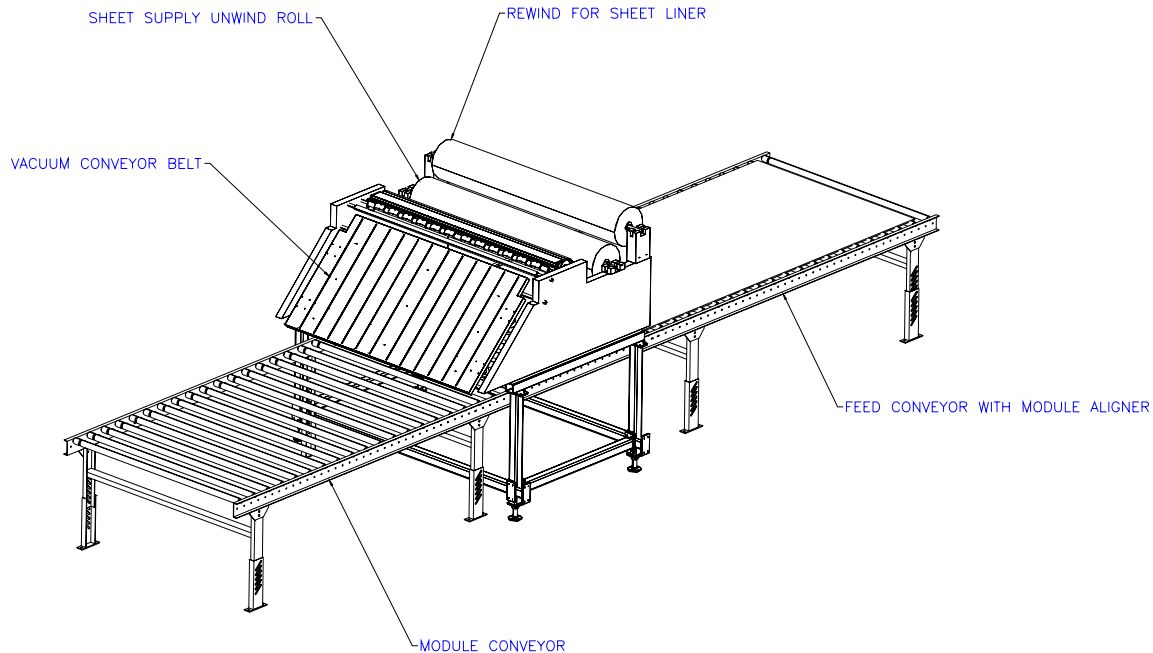


**Figure 38 Module conveyor with CSA sheeter configured for EVA dispensing on glass.**

## **2.5 Task 5 – Design String Busing System**

The design of a production prototype string busing system is underway at Spire, based on process evaluations done at ARRI. The system includes automation for transporting and aligning large area modules; feeding, cutting, punching, and placing bus ribbons; applying flux, placing diodes, and soldering bus ribbons to the diodes and cell strings. The string busing tasks are divided into two independent systems, one for prefabricating bus ribbons off-line, and one for installing bus ribbons and diodes in a module on an assembly line.

### **2.5.1 Bus Ribbon Fabrication**

Spire procured two types of copper bus ribbon with the proper dimensions and solder coating required for the Brightfield module design. Due to the high currents generated by the 800 W module, both ribbons are substantially wider (0.320” and 0.500”) than the widest ribbon we normally use in our 75 W modules (0.200”). The ribbons are wound on cardboard reels that contain roughly 5 kg (11 lbs) of ribbon per reel.

We set up a commercial ribbon feed-and-cut machine and a ribbon straightener to evaluate the bus ribbon feed, straighten, and cut processes. The machine uses a stepper motor with rubber rollers to dispense a measured amount of ribbon and a shear to cut it to length. Tests showed that the ribbon lengths varied and were shorter than selected. This indicates that the ribbon is slipping in the drive rollers, due to the drag from the heavy ribbon reel and the straightener. We designed larger drive rollers that apply more pressure on the ribbon to eliminate slipping.

The shear method is appropriate for the 0.320” wide ribbon, which is simply cut straight at both ends. However, the 0.500” wide ribbon needs a tab punched at one end and a straight cut at the other for connecting to the top and bottom surfaces of a diode. In this case, a punch and die are required to cut the ribbon instead of the shear. We considered modifying the existing machine to add a punch to the ribbon path in addition to the shear, but it was not possible to fit it in the space available, so we proceeded with a custom machine design.

Once the bus ribbon is cut or punched to length, it must be loaded into a tray that will hold a stack of ribbons. Most of the ribbon length will be pushed into the tray by the drive rollers, but the last several inches will remain in the shear or die set. We designed a two-axis pneumatic pick-and-place mechanism with a vacuum cup to pick up the trailing end of the ribbon, advance it so it is completely over the tray, and drop it into the tray.

It is important for the ribbon to remain relatively flat for stacking in the tray and for accurate assembly in the module. We were concerned that as the ribbon is pushed into the tray, the edges of the ribbon might rub on the tray sidewalls and bend, so we fabricated a prototype tray for 0.500" wide ribbon. Tests showed that the drive rollers reliably pushed the ribbon into the tray without distortion. Tests simulating the final pick-and-place operation were also successful in maintaining flat ribbon.

We designed a bus ribbon fabrication machine, shown in Figure 39, that feeds ribbon from reels, straightens it to remove coil set, cuts it to length, punches one end to form a tab for connecting to a diode, and fills trays with stacks of ribbon. Our module design requires three different lengths of ribbon, two with tabs for the diodes, all of which can be made automatically on this system. Mechanical assemblies and electrical controls were designed and are ready to release for fabrication in Phase 2 of the program.

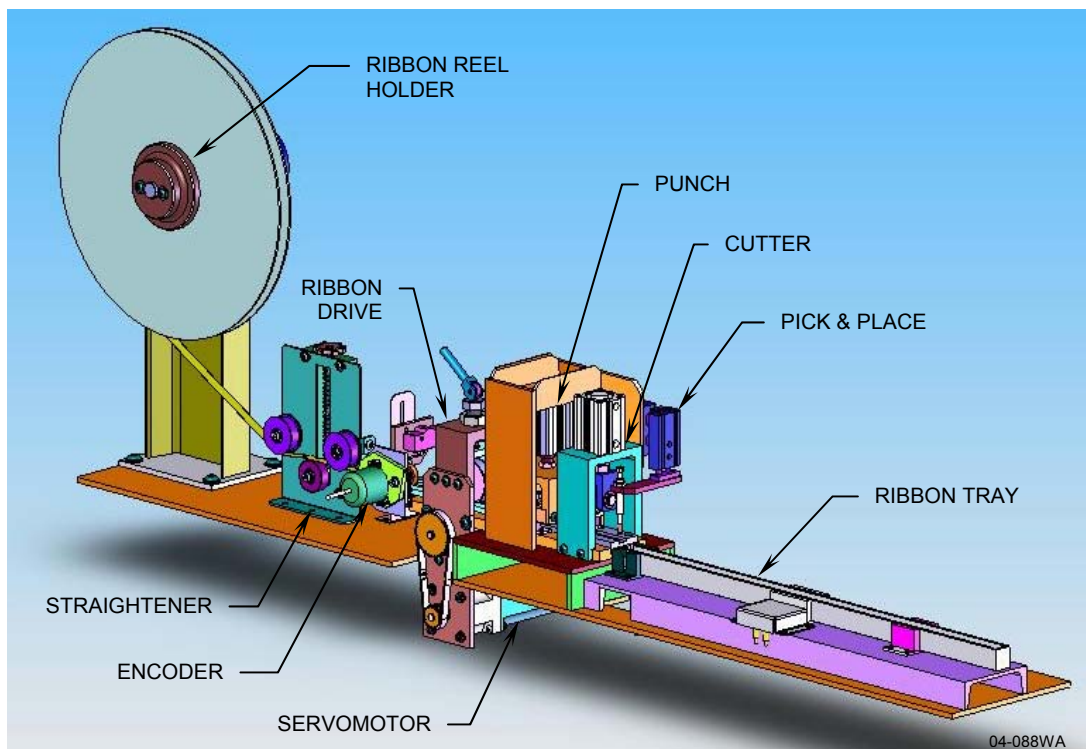


**Figure 39 Mechanical design for the bus ribbon fabrication machine.**

The ribbon reel holder has an adjustable magnetic clutch to prevent over-spin when the drive wheel pulls ribbon. The ribbon first passes through a straightener to remove coil set. The straightener consists of three unpowered rollers. The position of the center roller can be adjusted to press on the ribbon as required for straightening. The ribbon then enters a guide for alignment and passes under a spring-loaded wheel attached to an encoder, which monitors the ribbon for slip in the drive rollers. A lever and a limit switch are provided to sense when the reel runs out of ribbon.

The ribbon drive assembly consists of a spring-loaded pinch roller and a drive roller powered by a servomotor. A lever and cam lift the pinch roller up above the drive roller to simplify ribbon threading when a new ribbon reel is loaded.

The ribbon punch consists of a stationary die and an air-driven clamp and punch assembly. When the air cylinder is extended, the clamp holds the ribbon in place on both sides of the die while the punch cuts a tab shape on one end of the ribbon and a straight cut on the other end. The tab shape allows a connection to be made to the top surface of the diode without shorting to the bus ribbon connected to the bottom surface of the diode. The ribbon cutter assembly has a stationary blade and an air-driven blade that cuts across the ribbon as it moves down, like a paper cutter. The moving blade is spring-loaded against the stationary blade for self-alignment.

Once the bus ribbon is cut or punched to length, it is loaded into a tray that holds a stack of ribbons. Most of the ribbon length is pushed into the tray by the drive rollers, but the last several inches remains in the shear or die set. A two-axis pneumatic pick-and-place mechanism with a vacuum cup picks up the trailing end of the ribbon, advances it so it is completely over the tray, and drops it into the tray.

### 2.5.2 Bus Ribbon and Diode Installation – SCARA Robot Approach

The automation for bus ribbon and diode installation has gone through two design iterations. The first approach is based on a SCARA robot work cell similar to the one that ARRI used to develop the installation processes. In this approach, two SCARA robots, one on each side of the module, install bus ribbons and diodes, as shown in Figure 40. One third of the module is processed at a time, then the module is indexed forward on the conveyor to do the next third. This allows us to use moderate size robots with an 850 mm reach.

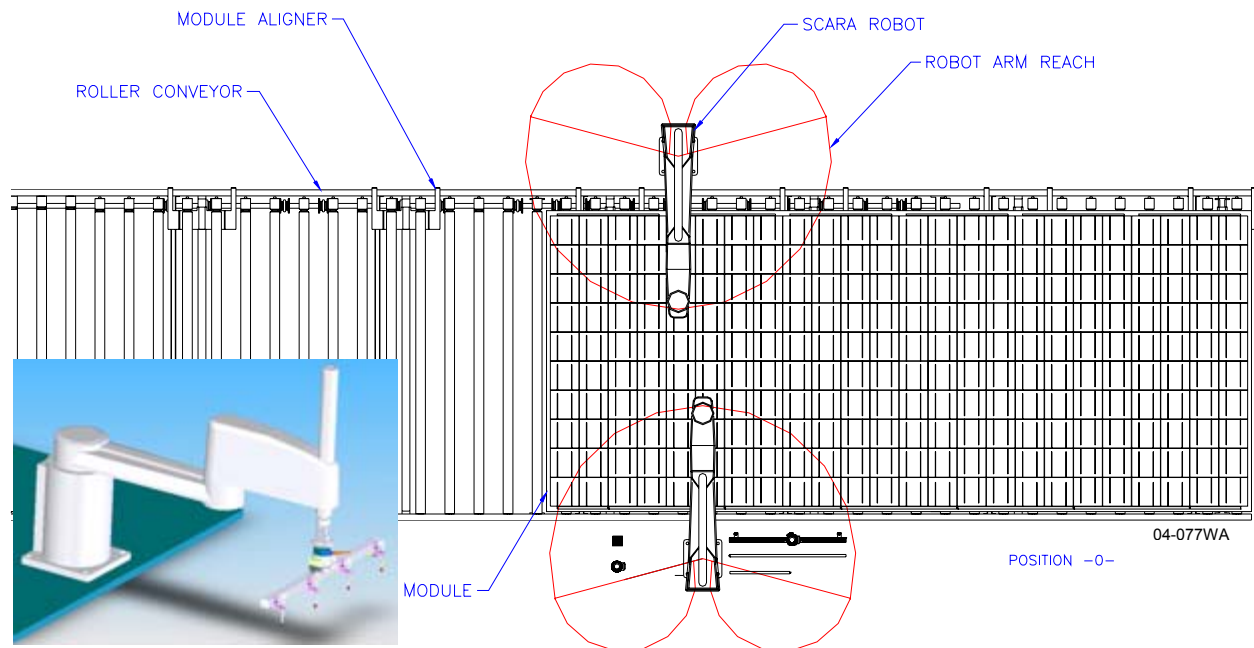


**Figure 40 SCARA robot approach to string busing (plan view). Inset shows a robot with a vacuum end effector for bus ribbon and diode handling.**

Each robot has a tool changer and two end effectors, one to pick and place components and another to solder connections between them. The pick and place end effector, shown in Figure 41, handles an insulating bar, bus ribbons of different lengths, and chip diodes, and assists with ancillary processing steps, such as bus ribbon bending and flux application. The insulating bar is temporarily placed on the module to allow the buses and diodes to be soldered without melting the EVA.

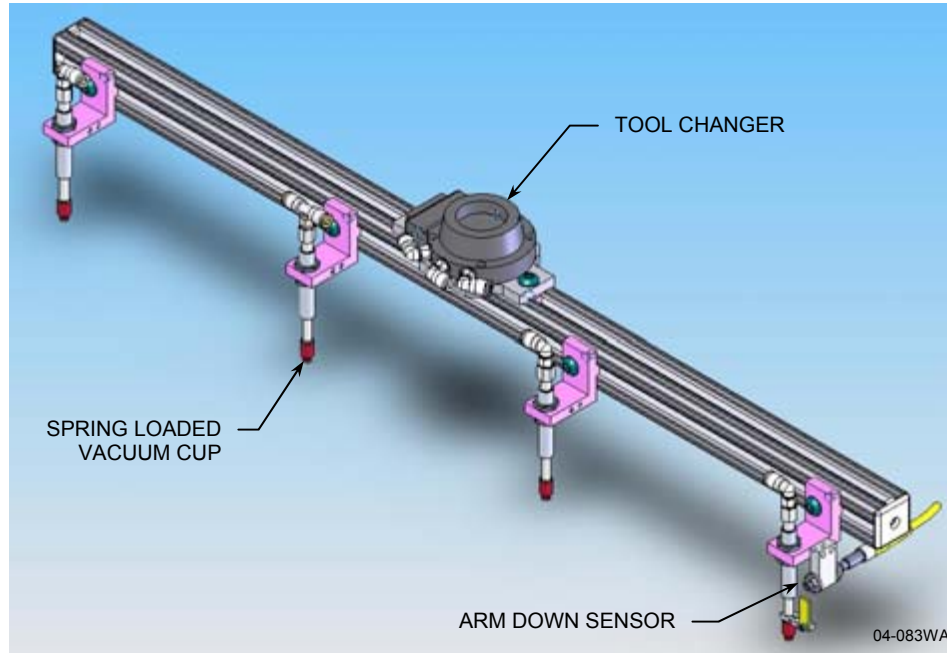


**Figure 41 Vacuum pick-and-place end effector design for robot arm.**

### **2.5.3 Bus Ribbon and Diode Installation – Cartesian Robot Approach**

An alternate approach for bus ribbon and diode installation uses a single Cartesian robot in place of the two SCARA robots. This approach is preferred if it has sufficient processing speed, because we can eliminate one robot and its tools, thereby reducing the system cost.

ARRI ran a computer simulation of the bus ribbon and diode installation process to determine the total cycle time for both methods. The simulation results show that the SCARA method, which uses two robots working simultaneously on opposite sides of the module, can complete a module in 5 minutes and 13 seconds. The Cartesian robot method, which uses a single robot for processing both sides of the module, can complete a module in 8 minutes and 49 seconds. A solar cell string assembly machine, producing at a rate of 600 cells per hour, will fabricate one Brightfield module (24 10-cell strings) in 24 minutes. Therefore, the Cartesian robot is more than fast enough to handle the output from two string assembly machines.

Since it is relatively easy to extend the axis lengths of a Cartesian robot, we designed the robot with sufficient reach to process the entire module in one position (i.e., without indexing). The robot has four axes: x, y, z, and  $\theta$  (rotation). The system design is shown in Figure 42.

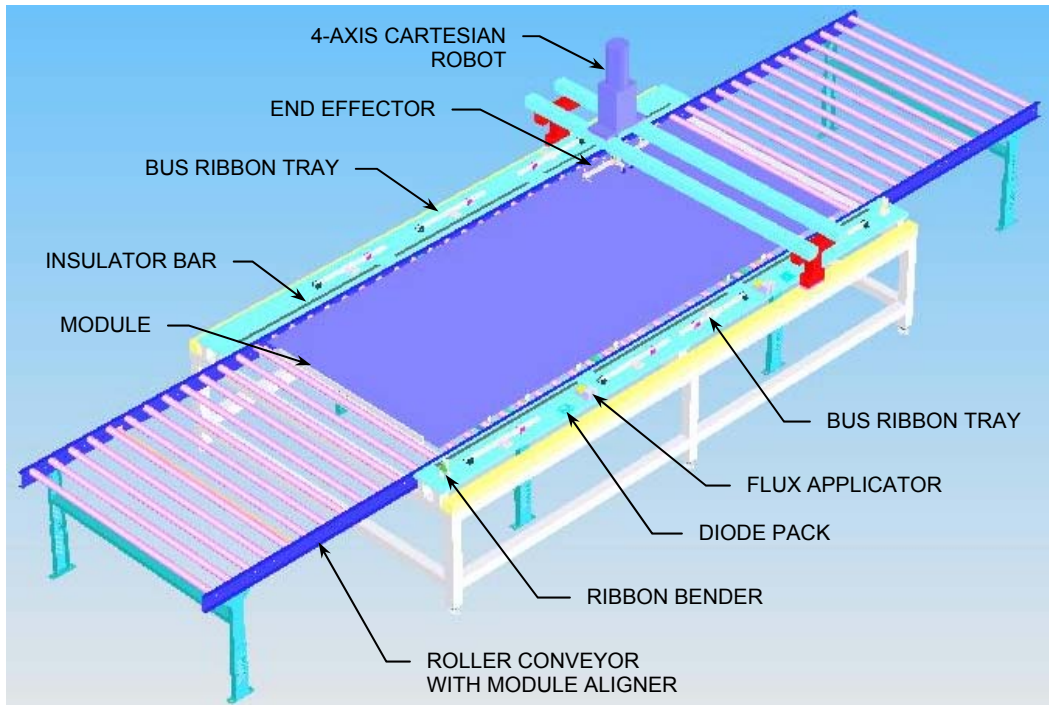


**Figure 42 Cartesian robot approach to string busing (perspective view).**

The ribbon tray assembly design is shown in Figure 43. The trays are filled by the ribbon fabrication machine (Figure 39), after which an operator transfers them to the string busing system (Figure 42). The assembly has an optical sensor located under a hole in each tray to detect when the tray is empty. Two proximity sensors detect steel pins inserted in the wall of the trays to determine which tray type is loaded. There are three tray types, one for each type of ribbon used in our module design.

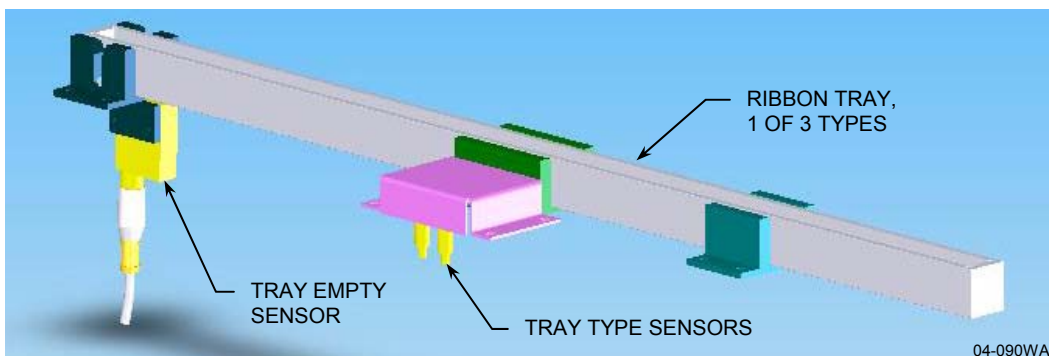


**Figure 43 Bus ribbon tray assembly (table not shown).**

A bus ribbon location tolerance study was done as part of the tray design. Given the large camber (in-plane curvature) specification provided by the ribbon supplier, the ribbon location tolerance is as large as  $\pm 1.19$  mm ( $\pm 0.047$  inch) in the ribbon width direction for the longest ribbon in our module. This tolerance is too large for aligning the bus ribbons to the diodes in the module, so the location of the ribbon ends must be determined after they are picked up from the tray by the robot. While a vision system could find the ribbon ends, we will use a fiber optic sensor, since the hardware is a significantly less expensive.

The robot end-effector design was reviewed and we were able to eliminate the tool changer by mounting the pick-and-place and the soldering tools on the same end effector, as shown in Figure 44. Eliminating the tool changer saves process time, end-effector complexity, and cost.

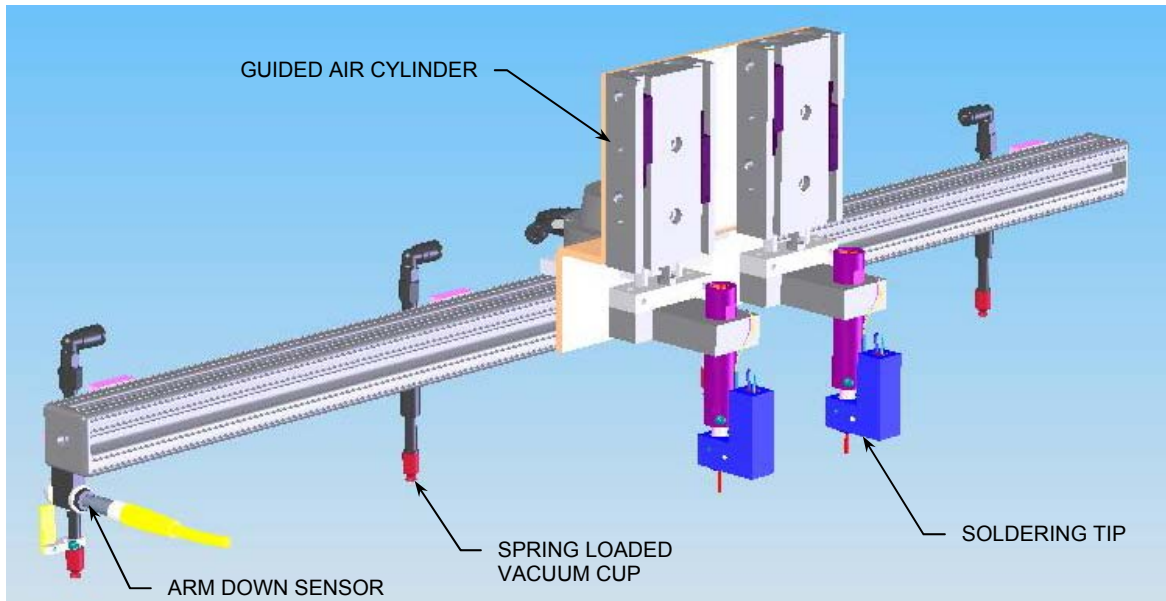


**Figure 44 Robot end effector with pick-and-place and soldering tools.**

The output bus ribbons at opposite ends of the module are bent up at a 90° angle to extend through the EVA and back sheet. A simple bus ribbon bending tool was prototyped at ARRI. The process sequence with ARRI's tool is illustrated in Figure 45. When the robot picks up an output bus, it places the end of the bus in a slot in the bending tool. A guided air cylinder pushes a plate over the ribbon to form a 90° bend. After the air cylinder retracts, the robot removes the ribbon from the tool and places it on the module.

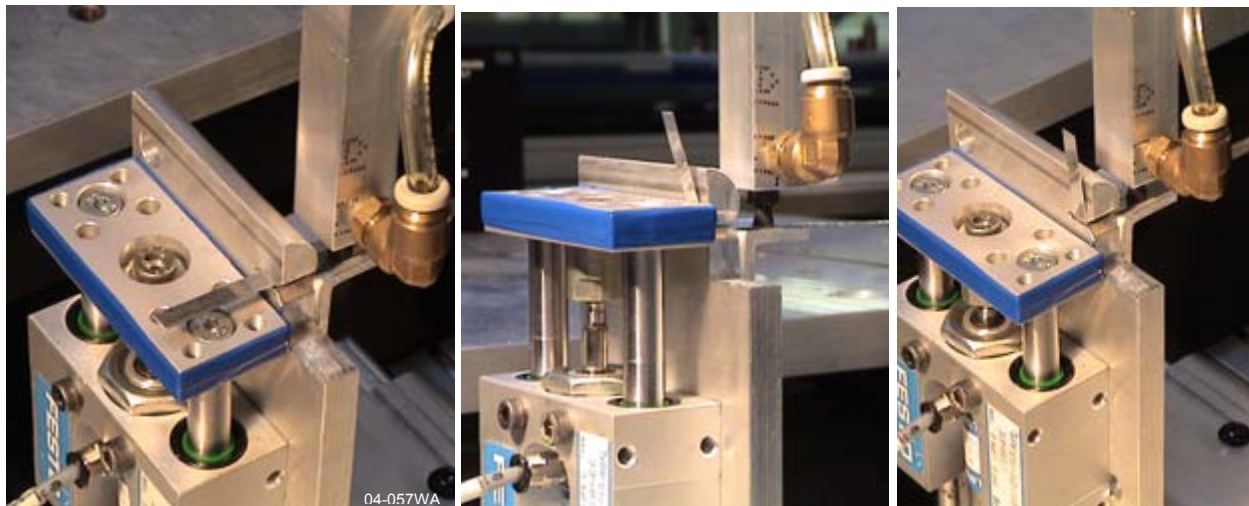


**Figure 45 A robot inserts a bus bar in the bending tool (left), an air cylinder extends to bend the ribbon (center), and the cylinder retracts (right).**

Spire designed a ribbon bending tool based on this concept. The tool, shown in Figure 46, uses a spring-loaded roller in place of the plate to form the bend in the ribbon. The roller eliminates scuffing or other damage that a plate might do to the ribbon, while the spring load allows the roller to follow the surface of the vertical plate without the need for precise alignment.

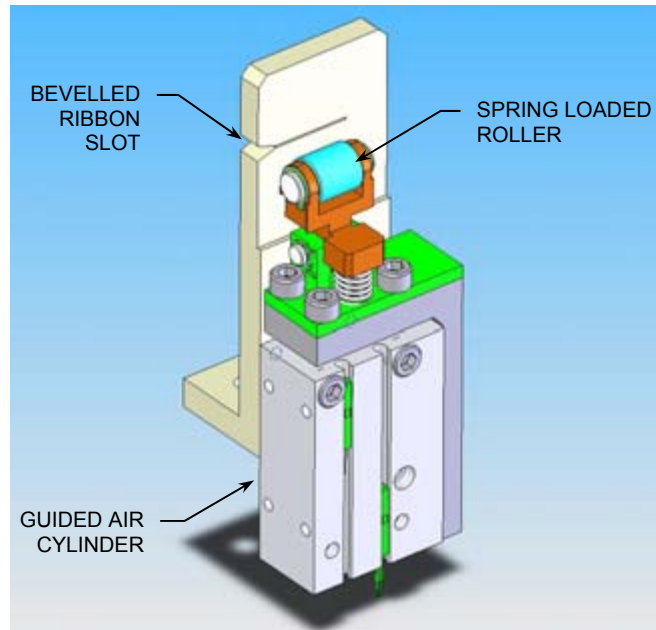


**Figure 46 Ribbon bender, Spire design.**

The by-pass diodes are solderable chips with silver contacts covering their top and bottom surfaces. A thin coating of flux must be applied at both (top and bottom) diode-bus ribbon interfaces for reliable soldering. ARRI demonstrated a robotic flux application method as follows. A robot with a vacuum end effector picks up a diode and places it momentarily on a sponge soaked in flux to coat its bottom surface. The diode is then placed on the appropriate bus ribbon in the module. Next, the robot picks up the bus ribbon that will contact the top of the diode and the end of the ribbon is momentarily placed on the sponge to coat its bottom surface. The ribbon is then placed with its fluxed end on the diode.

Spire then designed a flux applicator to implement this process. The applicator, shown in Figure 47, has a small flux reservoir, a float switch, a peristaltic pump, and a sponge. The float switch and the pump maintain a constant level of flux in the reservoir, roughly at the mid-point of the sponge thickness.

#### **2.5.4 Automated Soldering Process Development**

ARRI investigated reflow soldering techniques for soldering the bus ribbons to the diodes and cell strings. ARRI worked with Unitek Miyachi on pulsed hot bar reflow soldering equipment selection and design of a customized thermode for the soldering requirements specific to the Brightfield module, specifically the string-bus and bus-diode-bus joints. To simplify the soldering process both in terms of cycle time and cost, an effort was made to design a thermode head that is suitable for both joint types.

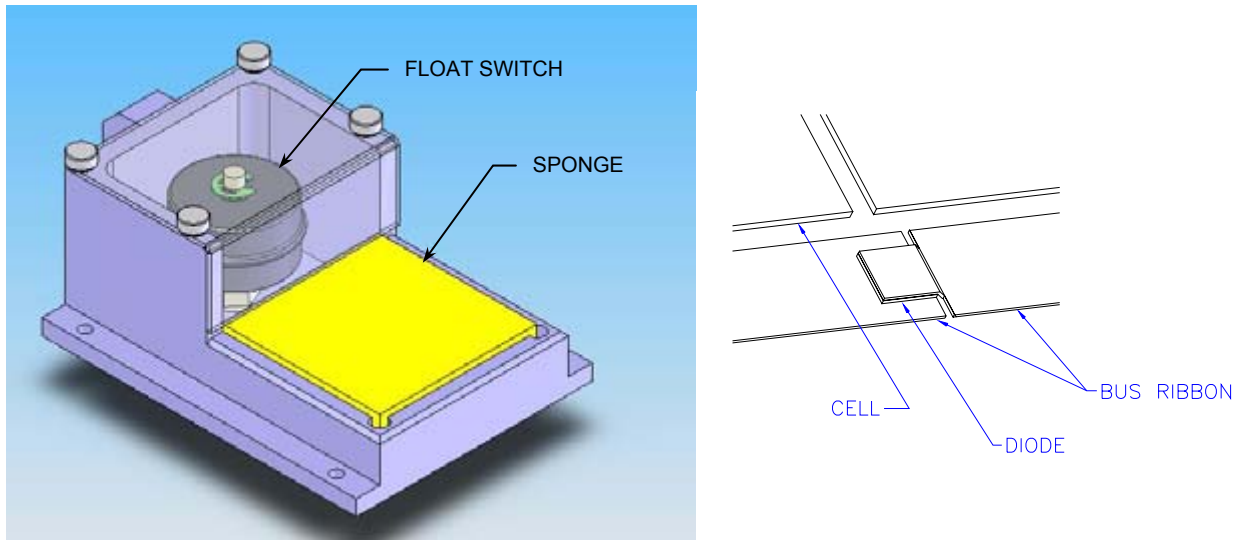


**Figure 47 Flux applicator (left) and diode assembly in the module (right).**

**String-bus soldering:** Due to the large number (96) of string-to-bus joints on the Brightfield module, a two-pronged thermode is recommended so that the two ribbons at the end of each cell string can be soldered in a single step. According to Unitek’s recommendation, a thermode head can be up to 130 mm wide and still maintain a constant temperature across the length of the head. The string lay-out on the module requires an 81.6 mm wide thermode head, well under the 130 mm limit. Testing at ARRI on string-to-bus joints showed that sufficiently sound joints can be formed with a thermode contact area of 2.2 mm × 3.0 mm. Each prong of the Unitek solder head would have dimensions of 7.2 mm × 3.0 mm, allowing for a variation in the position of the string on the bus of ±2.5 mm. A suggested thermode design is shown in Figure 48.

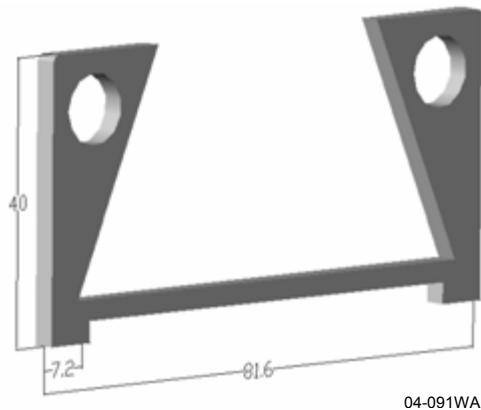


**Figure 48 Preliminary thermode design for string-bus and bus-diode-bus joints (dimensions in mm). Thickness is 3 mm.**

**Bus-diode-bus soldering:** ARRI sent tabbed, fluxed bus bars and diodes to Unitek Miyachi along with detailed drawings, and requested that they perform tests to determine what would be required (thermode design, power supply model, and reflow process) to form the bus-diode-bus joint in a single step. Unitek was able to solder the diode between the two bus bars, but did so using a two-step soldering process. Based on their testing, Unitek concluded that in order to form the bus-diode-bus joint in a single step, heating from both the top and bottom would be required. Unfortunately, this is not compatible with our

module automation approach, and it would almost double the cost of the soldering system due to the need for a second high current power supply.

ARRI continued feasibility testing on the bus-diode-bus joints using a temperature controlled industrial soldering iron as the heating source. Using a reflow temperature of 300 °C and a reflow time of 7 s, it was possible to obtain good solder bonds to the bus bars on both sides of the diode. With this method, the heat was applied only from the top.

The main drawback with a soldering iron is that it has no means for holding the solder joint in contact while the solder cools. This problem was recognized by Spire when we first started developing automated soldering equipment for solar cells twenty years ago. At that time, we invented a unique soldering tip that operates at a constant temperature and has a built-in pin that holds the joint in contact until the solder freezes. The soldering tip, shown in Figure 49, is heated by a small cartridge heater and its temperature is monitored by a thermocouple. The heated tip and the cooling pin are spring loaded for compliance with the soldered parts.

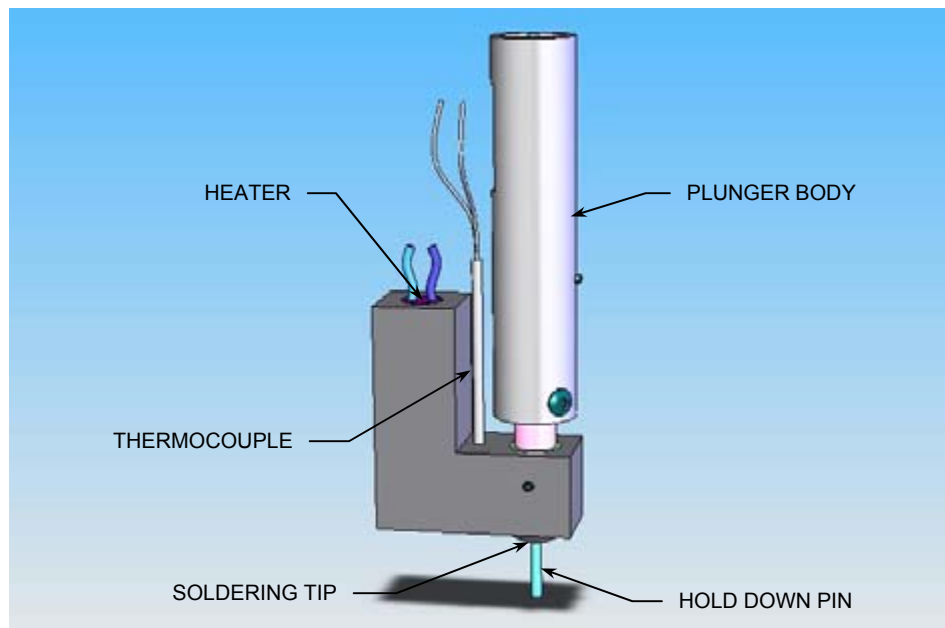


**Figure 49 Spire soldering tip assembly.**

A low-cost PID temperature controller is all that is needed for controlling the Spire solder tip. Since the heater operates at low current, it eliminates the massive cables needed by the pulsed hot bar soldering system. This is a significant advantage, since the solder tips are mounted on a robot, where the mass must be minimized. Given the substantial cost savings and reduced mass of the controls, the Spire designed solder tip was selected for this application.

Two solder tips are shown mounted on the robot end effector in Figure 44. This allows the two ribbons at each end of each string to be soldered to the bus ribbon at one time. Each tip is mounted on a guided air cylinder to keep them retracted when they are not in use, i.e., when the robot is performing pick-and-place operations. A single tip will be extended for diode soldering.

### **3 CONCLUSIONS**

Spire has completed the first phase of a three-phase program for developing automated production line processes for solar Brightfield modules. A large area 800 W module for utility-scale PV arrays was designed, with emphasis on minimizing BOS costs. Unique module features include internally laminated by-pass diodes, which greatly simplified the internal busing and the output terminals, and a cantilevered superstrate that allowed for a reduced glass thickness and a simpler frame design.

The design of automated tools is underway for producing such modules in multi-megawatt per year quantities. A cell string inspection system with machine vision and microcrack detection capabilities was developed and tested. Spire applied for a patent on the infrared crack detection technique. An advanced lamination process was developed with a faster-curing EVA for increased laminator throughput, and efforts are underway to reduce laminator maintenance and downtime. Automated systems are being designed for dispensing and laying up module materials (EVA and back sheet) and for installing and soldering bus ribbons and diodes prior to lamination.

In the remaining two phases of our program, we plan to fabricate and test the automated module lay-up and string busing systems; design, fabricate and test an improved laminator and a large area sun simulator; and develop a computer integrated manufacturing system for module line supervisory control and data acquisition.

# REPORT DOCUMENTATION PAGE

*Form Approved*  
OMB No. 0704-0188

The public reporting burden for this collection of information is estimated to average 1 hour per response, including the time for reviewing instructions, searching existing data sources, gathering and maintaining the data needed, and completing and reviewing the collection of information. Send comments regarding this burden estimate or any other aspect of this collection of information, including suggestions for reducing the burden, to Department of Defense, Executive Services and Communications Directorate (0704-0188). Respondents should be aware that notwithstanding any other provision of law, no person shall be subject to any penalty for failing to comply with a collection of information if it does not display a currently valid OMB control number.

**PLEASE DO NOT RETURN YOUR FORM TO THE ABOVE ORGANIZATION.**

<b>1. REPORT DATE (DD-MM-YYYY)</b> June 2005		<b>2. REPORT TYPE</b> Subcontract Report		<b>3. DATES COVERED (From - To)</b> 1 January 2003–30 June 2004		
<b>4. TITLE AND SUBTITLE</b> Development of Automated Production Line Processes for Solar Brightfield Modules: Annual Technical Progress Report, 1 January 2003–30 June 2004			<b>5a. CONTRACT NUMBER</b> DE-AC36-99-GO10337			
			<b>5b. GRANT NUMBER</b>			
			<b>5c. PROGRAM ELEMENT NUMBER</b>			
<b>6. AUTHOR(S)</b> M.J. Nowlan, J.M. Murach, S.F. Sutherland, D.C. Miller, S.B. Moore, and S.J. Hogan			<b>5d. PROJECT NUMBER</b> NREL/SR-520-36608			
			<b>5e. TASK NUMBER</b> PVB56101			
			<b>5f. WORK UNIT NUMBER</b>			
<b>7. PERFORMING ORGANIZATION NAME(S) AND ADDRESS(ES)</b> Spire Corporation One Patriots Park Bedford, Massachusetts 01730-2396				<b>8. PERFORMING ORGANIZATION REPORT NUMBER</b> ZDO-2-30628-12		
<b>9. SPONSORING/MONITORING AGENCY NAME(S) AND ADDRESS(ES)</b> National Renewable Energy Laboratory 1617 Cole Blvd. Golden, CO 80401-3393				<b>10. SPONSOR/MONITOR'S ACRONYM(S)</b> NREL		
				<b>11. SPONSORING/MONITORING AGENCY REPORT NUMBER</b> NREL/SR-520-36608		
<b>12. DISTRIBUTION AVAILABILITY STATEMENT</b> National Technical Information Service U.S. Department of Commerce 5285 Port Royal Road Springfield, VA 22161						
<b>13. SUPPLEMENTARY NOTES</b> NREL Technical Monitor: K. Brown						
<b>14. ABSTRACT (Maximum 200 Words)</b> This report describes how Spire Corporation is addressing the PV Manufacturing R&D project goals of improving photovoltaic (PV) manufacturing processes and products while reducing costs and providing a technology foundation that supports significant manufacturing scale-up. To accomplish this, we are focusing our efforts on the design of a large-area utility-scale module and the development of the necessary manufacturing techniques and equipment to manufacture such a module in a high-volume production environment. A three-phase program is under way for developing and demonstrating new automated systems for fabricating very large PV modules ideal for use in multi-megawatt grid-connected applications. We designed a large-area 800 W module and we are developing associated module production equipment that will minimize the total installed system cost for utility-scale PV arrays. Unique features of the module design include a cantilevered glass superstrate to reduce the glass thickness and internally laminated bypass diodes that simplify internal busing and junction-box designs. Other program activities include the development of automation for solar cell string inspections, string busing, materials lay-up, and lamination; enhancements to the lamination process; and performance testing of large-area modules.						
<b>15. SUBJECT TERMS</b> PV; manufacturing; solar cell; utility-scale module; string inspections; string busing; materials lay-up; lamination; manufacturing scale-up; high-volume production; automated systems; large-area module;						
<b>16. SECURITY CLASSIFICATION OF:</b>			<b>17. LIMITATION OF ABSTRACT</b>  UL	<b>18. NUMBER OF PAGES</b>	<b>19a. NAME OF RESPONSIBLE PERSON</b>	
<b>a. REPORT</b> Unclassified	<b>b. ABSTRACT</b> Unclassified	<b>c. THIS PAGE</b> Unclassified			<b>19b. TELEPHONE NUMBER (Include area code)</b>	